Montanuniversität Leoben

Comparison of Magnetron Sputtering and Arc Evaporation by Al-Cr-N hard coatings

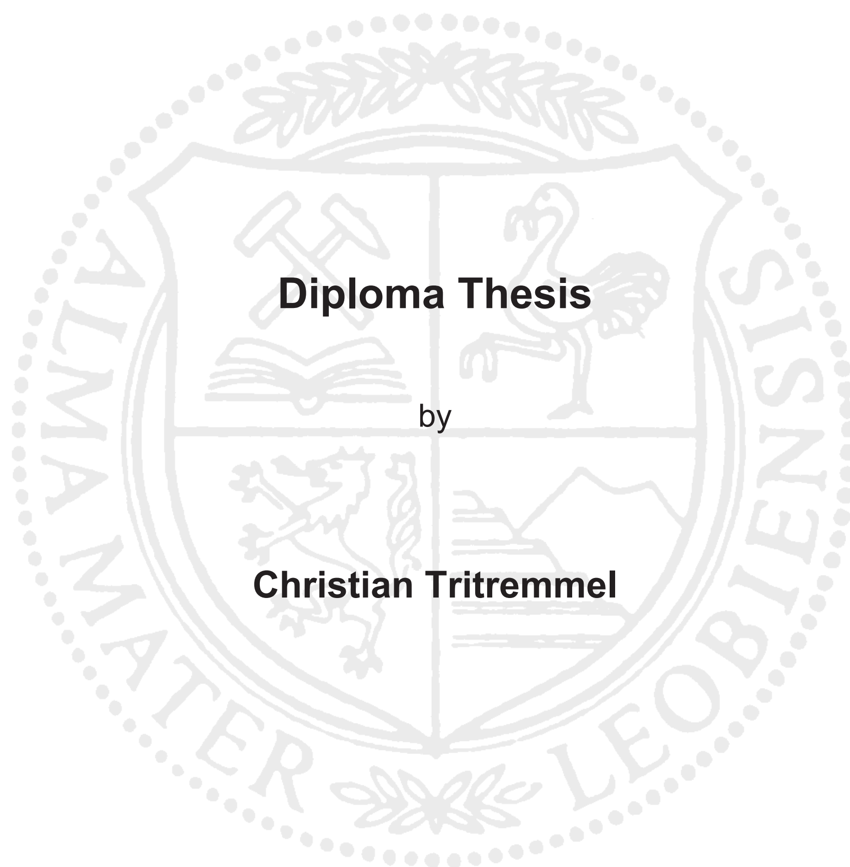

Diploma Thesis

by

Christian Tritremmel

accomplished at the

Department of Physical Metallurgy and Materials Testing in corporation with the Christian-Doppler-Laboratory for Advanced Hard Coatings

Leoben, June 2007

Acknowledgements

First of all I would like to thank Univ.-Prof. Dr. Helmut Clemens, head of the Department of Physical Metallurgy and Materials Testing, for the opportunity to carry out this diploma thesis at his department.

Special thanks also to a.o. Univ.-Prof. Dr. Christian Mitterer, head of the thin film group and head of the Christian Doppler Laboratory for Advanced Hard Coatings, for giving me the chance to write about this topic.

My sincerest gratitude is due to my supervisor, Dr. Jörg Neidhardt, for his great support and kindness and of course for his expertise giving to this diploma thesis.

I also want to thank the members of the department for their help in investigations and of course for the useful discussions.

I am also grateful for the support received from Oerlikon Balzers Coating, especially from the staff in Kapfenberg.

Finally I want to thank my parents for the possibility studying at the University in Leoben.

Table of contents

1 Introduction ... 1
2 Plasma assisted physical vapour deposition techniques ... 3
  2.1 General ... 3
  2.2 Plasmas ... 4
    2.2.1 Plasma analysis ... 6
  2.3 Magnetron sputtering ... 11
  2.4 Cathodic arc evaporation ... 16
3 Coating formation ... 19
  3.1 General ... 19
  3.2 Nucleation and growth ... 19
  3.3 Structure zone models (SZM) ... 21
4 Experimental ... 24
  4.1 Coating synthesis ... 24
    4.1.1 Deposition plant ... 24
    4.1.2 Targets, gases, substrates ... 25
    4.1.3 Deposition procedure ... 26
    4.1.4 Magnetron sputtered coatings ... 28
    4.1.5 Arc evaporated coatings ... 29
  4.2 Coating analysis techniques ... 31
    4.2.1 Coating thickness ... 31
    4.2.2 Scanning electron microscopy (SEM) ... 32
    4.2.3 Optical profilometry (white light interferometer) ... 32
    4.2.4 X-Ray-Diffraction (XRD) ... 33
    4.2.5 Biaxial stress temperature measurements (BSTM) ... 35
    4.2.6 Nanoindentation ... 37
  4.3 Plasma investigations ... 40
    4.3.1 Planar probe measurement ... 40
5 Results and discussion ... 43
  5.1 Coating synthesis ... 43
    5.1.1 Thickness and growth rate ... 43
  5.2 Coating morphology ... 47
    5.2.1 Magnetron sputtered coatings ... 47
    5.2.2 Arc evaporated coatings ... 48
  5.3 Coating structure ... 51
    5.3.1 Phase fraction, lattice parameter ... 55
  5.4 BSTM measurements ... 56
    5.4.1 Residual stresses ... 56
    5.4.2 Linear thermal expansion coefficient ... 59
  5.5 Nanoindentation (hardness and modulus) ... 61
    5.5.1 Magnetron sputtered coatings ... 61
    5.5.2 Arc evaporated coatings ... 62
    5.5.3 Comparison of sputtered and arced coatings ... 64
  5.6 Plasma investigations ... 65
    5.6.1 Magnetron sputtered coatings ... 65
    5.6.2 Arc evaporated coatings ... 70
    5.6.3 Comparison of arc evaporated and sputtered coatings ... 74
6 Summary ... 76

7 List of tables and figures 79
7.1 List of tables...79
7.2 List of figures 80
8 References 82

1 Introduction

The increasing importance of hard coatings is attributed to the higher demands on coated tools and components. Therefore, there is a need for the development of already well established coatings and also a search for new hard coatings with improved properties. Characteristics, such as high hardness, good oxidation resistance, low friction and wear coefficient are important features, which are benchmarks for this coating development. Recent studies on arc evaporated Al-Cr-N coatings have shown that this material is a good candidate as an alternative to conventional CrN coatings and as such has been (introduced to the market a few years ago) commercialized [1, 2]. Al-Cr-N is a rather modern coating with increased oxidation resistance and high hardness [3]. The thermal stability allows applications up to 1000°C [4]. Economic considerations established arc evaporation as the most common industrial synthesis route, due to its high degree of ionisation and high deposition rates. However, arc evaporation has a main disadvantage: molten globules (droplets) ejected from the electrode can be deposited in the film, causing growth defects on the surface. These droplets, inherent to arc evaporation, can act as diffusion channels and phase transformation nucleation sites and as such limit the oxidation resistance as well as mechanical integrity [5]. Magnetron sputtering in turn is droplet free but suffers from a much lower degree of ionization and lower deposition rates. Therefore, this study is focused on a comparison of coatings synthesised by arc evaporation and magnetron sputtering under industrial conditions in a commercial deposition plant (Balzers RCS).

At first it is necessary to establish the parameters for a comparable coating synthesis by sputtering as well as arc evaporation. The adjustments include in addition to the target composition the values of the sputter power, bias voltage, nitrogen gas flow during deposition, the coating time and of course the deposition temperature. The ion bombardment during the film growth originating from the plasma plays an important role in the morphology, structure and mechanical properties of thin films. This ion bombardment can be controlled by biasing the substrate. Based on these considerations different AlCrN coatings were deposited using both, magnetron sputtering and arc evaporation techniques.

The target composition was varied from 25 over 70 to 85at% Al in the Al/Cr targets (cathodes), to investigate the transition from the metastable cubic phase to the stable hexagonal (hex) phase. This transition might also be affected by the energy supplied to the growth surface. For that reason the bias voltage was adjusted from -40 to -150 V. The resulting coatings were analyzed as to their microstructure, composition and mechanical properties by, e.g., X-ray diffraction in combination with Rietveld refinement, electron probe micro-analysis and nanointendation.

Additionally a process analysis was carried out. This includes the evaluation of the incorporation rate by using the deposition rate and the density of the coating. Furthermore via planar probes, plasma characteristics such as floating potential and ion flux density were determined for both deposition techniques.

2 Plasma assisted physical vapour deposition techniques

2.1 General

For the deposition of thin hard coatings physical vapour deposition (PVD) techniques are besides chemical vapour deposition (CVD) the most common procedures. PVD processes include the following main types: evaporation, sputtering and the reactive versions from the above named procedures. These techniques are used to deposit coatings on a substrate to improve for example optical, mechanical and chemical properties.

A variety of the PVD-techniques exists using different effects for the deposition of thin films. The methods differ in the physical state of the coating material as well as in the external conditions. In comparison to chemical vapour deposition processes (CVD), where the process temperature depends on the reaction temperature; the substrate temperature in PVD-processes is free selectable [6]. Another feature of the PVD techniques is the variety of the substrate materials, such as metals, alloys, glasses and plastics. In addition a nearly “unconfined” selection of coating compounds is possible, including carbides, nitrides and metal oxides [7]. Coatings, generated with PVD methods are known for their excellent film adhesion and the microstructure of the coating can simply be influenced by the choice of process parameters. On the other hand only comparatively low deposition rates and coating thicknesses can be achieved with PVD. Another disadvantage is that for the realization of the deposition process a vacuum is necessary. Expressed in other words, PVD-procedures are technically demanding processes. But the main disadvantage compared to CVD is that the deposition of geometrically complex components is challenging [6]. Both PVD and CVD processes are accomplished in controlled atmosphere.

In this work magnetron sputtering and arc evaporation were used. PVD processing is carried out in an evacuated chamber, backfilled with process gas, and at temperatures which can vary over a wide range. During the deposition process a reactive gas can be introduced (e.g. nitrogen). The high-purity, solid coating material (e.g. titanium, chromium or aluminium) is either evaporated by an arc discharge (arc evaporation, see section 2.4) or by bombardment with ions (sputtering, see section 2.3). During sputtering, the particles are knocked from the target (coating material) by means of accelerated inert gas ions (Ar). The energy transfer occurs due to interaction between the high energetic incident particles and the surface atoms of the target.

In the arc evaporation mode, the cathode surfaces are vaporized by an localized high current discharge and form a plasma of the vaporized material. After transformation to the vapour phase, the gas phase transport between source and substrate follows.
As last step, the condensation, nucleation and growth reaction with activated reactive gas takes place on the substrate surface (details in section 3). The result should be a thin, highly adherent coating. In order to obtain a uniform coating thickness, complex shaped parts are rotated at uniform speed around several axes, for industrial processes.
As mentioned before the whole process takes place in vacuum, to ensure that the evaporated atoms reach the substrate surface and reactions with unwanted residual gases are excluded. The evacuation of the deposition chamber minimizes the possibility of collisions on the way to the substrate surface due to removing of residual gases. In a vacuum the plasma provides a source of ions and electrons (from the process gas), that may be accelerated to high energies in an electric field. The plasma gives the great advantage of coupling non-thermal energy from an electric field into the film deposition process [8].

2.2 Plasmas

Plasma is often called the fourth state of matter. Rosén et al. describes the plasma as a partially ionized gas, consisting of atoms, electrons and ions [9]. A plasma consists of equal positive and negative charges, that means it is electrical conductive but on the other hand it seems to be neutral. Opposite to the physical plasma state, which appears at high temperatures and high pressures giving ions and electrons the same energy, these process plasmas are produced by ionization and therefore they are called low pressure plasmas. Another name for these plasmas is “cold plasmas” [10, 11]. This notation is valid due to the much lower ion temperature (0.02 to 0.1eV) compared to the electron temperature (> 1eV). In many plasma coating applications positive ions are generated by collisions between neutral particles and energetic electrons. The electrons in the plasma are highly mobile, especially compared to the larger ions (typically argon for sputtering). Control of these highly mobile plasma electrons is the key to all forms of plasma control. When establishing plasma in a vacuum, the gas pressure plays an important role due to the influence on density of charged and uncharged particles. The easiest method to generate an ion bombardment is to maintain a glow discharge between the target as cathode and the substrate as anode. Fig 2.1 shows the voltage-current characteristics of a gas discharge between the electrodes [11, 12].

Three general regions can be identified: the dark discharge region, the glow discharge, and the arc discharge.

The region between A and E on the voltage-current characteristics is termed a dark discharge, because the discharge remains nearly invisible to the eye. Within this part the current density is rather low ($\leq 10^{-6}$A). This part of the voltage-current characteristics is also called as Townsend regime.

Further increase of the current density leads to a visible glow discharge by exceeding the breakdown voltage. This voltage is influenced by the product of gas pressure and electrode separation (Paschen law) [13]. The feature of the glow discharge is the luminous looking plasma. The "glowing" results from inelastic collisions of electrons with an energy high enough to generate visible light by excitation collisions [10].

The glow discharge regime can be divided in normal and abnormal glow. Within the normal glow discharge, the voltage is independent of the current. At low currents only a small part of the cathode surface is in contact with the plasma [11]. Increasing the current to point G (Fig. 2.1), signifies that the plasma covers the whole cathode surface [12]. Up to this point the voltage remains constant. Further increase in current results in a significant rise of voltage.

This is a feature of the abnormal glow discharge. The applications of abnormal glow discharge include magnetron sputtering used for depositing thin films. Following to the abnormal glow region, which ends at the point of maximum voltage (H), the arc discharge regime occurs. At this point the voltage is breaking down by an arc discharge [11]. The arc regime, from I through K is one where the discharge voltage decreases as the current increases, until large currents are achieved at point J, and after that the voltage increases slowly as the current increases [12].

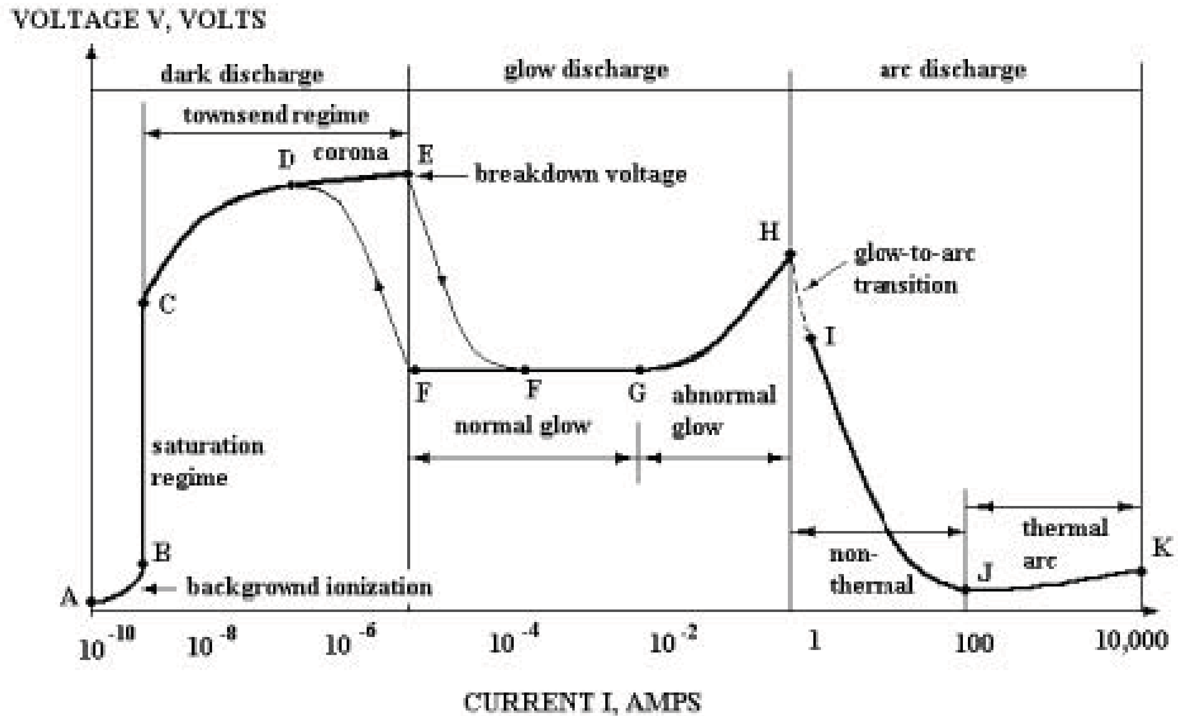

Fig. 2.1 Voltage-current characteristics of a gas discharge [12]

The collapsing of the discharge is localized at the cathode surface causing the evaporation of particles.

As mentioned before, an abnormal glow discharge is necessary for the sputtering process. The free electrons which are essential for this discharge are mainly generated by two processes. One sequence is the impact ionisation of electrons with gas molecules (volume ionization) and the second process is the emission of electrons from the cathode by means of ion bombardment (surface ionization) [13].

2.2.1 Plasma analysis

Prior to describing the plasma diagnostics, a few fundamentals of plasmas will be mentioned. Basically the various states of matter occur at different temperatures (energy levels). As a result, for the highest energetic state the binding energies of electrons is exceeded and thereby electron and ions are generated. Reaching the plasma state means that the charged particle density of electrons (n_e) and ions (n_i) are equal (eq. 1).

$$n_e = n_i = n_{pl} \tag{1}$$

n_{pl} is the plasma density and means the particles per m^3. In the plasma state a significant fraction of the atoms are dissociated into electrons and positively charged ions to form an ionized gas. The fraction of the atoms that are dissociated is called the degree of ionization (X_{di}) shown in eq. (2).

$$X_{di} = \frac{n_i}{n_g + n_i} \quad (2)$$

In this equation n_g is the neutral gas density. If X_{di} is 1 then the plasma is fully ionized. On the other hand if $X_{di} << 1$ then a weakly ionized plasma exists [14].
For the diagnostics of plasma properties numerous techniques exist. Basically it must be distinguished between two measuring systems. On the one hand non-invasive techniques, which operate contactless (e.g. emission spectroscopy) [8]. The second system uses invasive methods, which are in direct contact with the plasma being measured. Most of them are based on electric methods due to the simple experimental set-up [8, 15].

Within this diploma thesis plasma measurements were carried out to investigate the influence of synthesis technique and conditions on floating potential and ion flux density (see section 4.3). In the following, electric probes will be commented. An electric probe (Langmuir probe) is a small electrode, which is brought into the plasma. On it a variable potential is applied and the resulting current, measured on the probe is the sum of ion and electron current. In most cases the probe is a thin wire, because of the lower disturbance of the plasma. These kinds of probes are denoted cylindrical probes. But they also could be of spherical or planar geometry [15]. In this work the probes used have planar shape. Detailed information about the planar probes is given in the experimental part of this thesis (section 4.3). The easiest proceeding to get information about the plasma is to measure the voltage-current characteristics of the discharge.

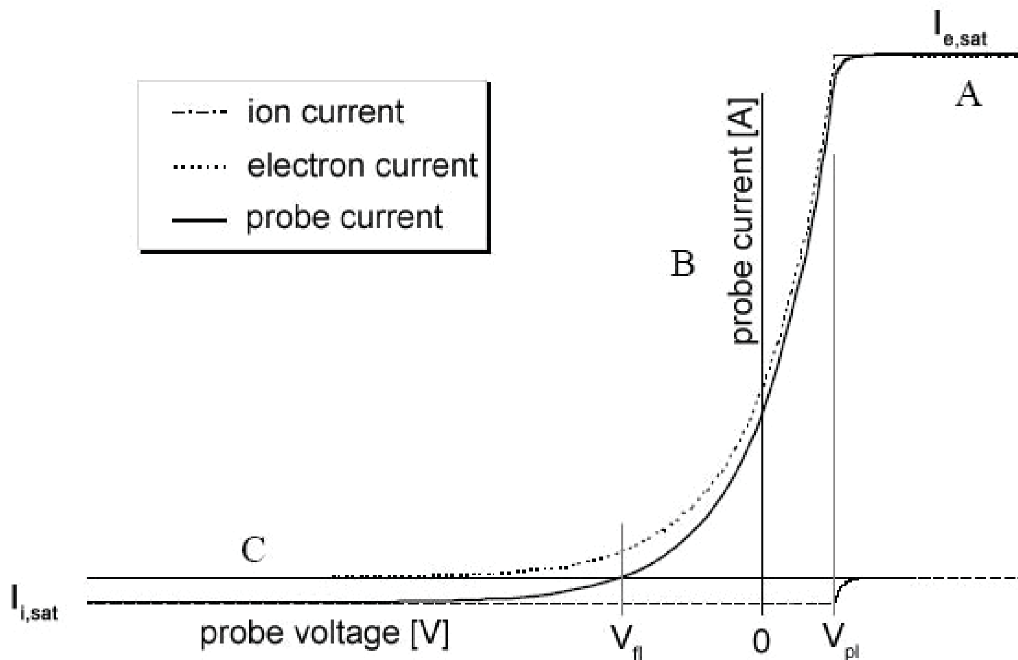

Fig. 2.2 Illustration of an V-I-curve of a plasma as probed with planar probes [15]

In Fig. 2.2 an ideal voltage-current curve of a plasma probed with planar probes is shown. Basically the curve can be divided into three regions; the electron dominated region (A) at a positive voltage, the transition region (B) and the ion dominated part (C) at negative voltages [16]. At higher positive voltages only electrons are extracted from the plasma in the electron saturation (region A) [15]. Due to the higher mobility of the electrons the electron current is much larger than the ion one, at comparable positive and negative voltages. For the same reason the potential of the plasma is always positive, since electron are much more likely to strike a surface leaving an apparently ion-rich and, thus, positive bulk plasma behind. If the probe is exactly at the potential of the plasma (V_{pl}), then only the thermal flux of electrons and ions are collected (deflection point of the I/V curve). Increasing the probe potential to a value more negative than the plasma potential, electrons are gradually repelled depending on their kinetic energy, and ions get attracted by the more negative voltage (transition region B) until the point is reached, at which the electron current and ion current are equal [15]. As consequence the probe current is zero. The potential that arises is referred to as the floating potential (V_{fl}), which is equivalent with the potential on an unbiased probe. If the probe is biased still more negatively, then finally only ions reach the probe (ion saturation, range C) [15]. $I_{e,sat}$ is the current at a potential higher than the plasma potential and $I_{i,sat}$ is the ion saturation current.

As can be seen from Fig 2.2 the probe current (I_{pr}) is the sum of electron (I_e) and ion current (I_i),

$$I_{pr} = I_e + I_i \tag{3}$$

In this work the plasma measurements were carried out applying a negative bias voltage and therefore the electron current becomes negligible and the current is given by the ion current [17]. With the measured ion saturation current ($I_{i,sat}$) the ion flux density can be calculated (section 4.3).
In the following the plasma potential and the floating potential are accurately described [18].

Plasma potential

Because of the much higher mobility of electrons in plasmas compared to ions, the first will tend to reach the borders of the plasma at a faster rate than the latter. If a plasma is somehow created and sustained in a metal vacuum chamber, the electrons would leave the plasma at a faster rate than ions, to, e.g., the walls of the vacuum system. The result for the plasma would be a slow increase in the net positive charge.
As the plasma charges positively, it becomes less energetically, favourable for the electrons to leave, because now the walls of the chamber are more negative than the plasma.
Eventually, a steady state condition would be reached in which the plasma potential is high enough that the loss rate of electrons is reduced to the same level as the loss rate of ions. In this way the plasma will retain its overall neutrality.
The plasma potential, which is now the average potential of the bulk plasma with respect to the chamber, will be on the order of several volts more positive than the chamber potential. This result is found in all processing plasmas: the plasma potential, on the average is a minimum of several Volts more positive of the most positive surface in contact with the plasma. As a result of this plasma potential, ions that reach the edge of the plasma are then accelerated with the same voltage to the chamber wall. The energy of this ion bombardment is usually too small to cause physical sputtering, but is very efficient in dislodging weakly bound absorbents from the chamber wall. In eq. (4) the derivation of the plasma potential (V_{pl}) from the voltage-current-curve is shown [19].

$$\frac{d^2 I}{d^2 V} = 0 \tag{4}$$

Floating potential

If an electrically floating surface is placed in contact with the plasma, it will rapidly charge negatively because of larger flux of electrons compared to ions. At some point, the surface will be sufficiently negative that enough electrons will be repelled to cause an equal flux of ions and electrons. The potential on this surface is known as the floating potential (V_f) and it is typically negative of the plasma potential. It is given by eq. (5).

$$V_f = -\frac{k_B T_e}{2e} \ln\left(\frac{m_i}{2\pi\, m_e}\right) \tag{5}$$

Here, m_e and m_i are the electron and ion masses, T_e is the electron temperature and k_B is the Boltzmann constant. The smaller electron mass results in a higher mobility of the electrons and therefore the electron temperature is much higher compared to the ion temperature. Consequently the number of ions (n_i) can be determined from the following eq. (6), if V_f, I_0 and T_e are known.

$$I_0 = n_i \sqrt{\frac{k_B \cdot T_e}{2\pi \cdot m_i}} \tag{6}$$

2.3 Magnetron sputtering

Ions with sufficient energy striking on a solid surface cause among other interactions the emission of atoms, clusters or molecules of the bombarded material. That means the physical sputtering process is a non thermal vaporization process in which target atoms are ejected by means of momentum transfer of bombarding (ionized) atoms [13]. This atomizing is the principle behind the widespread sputtering process (Fig. 2.3).

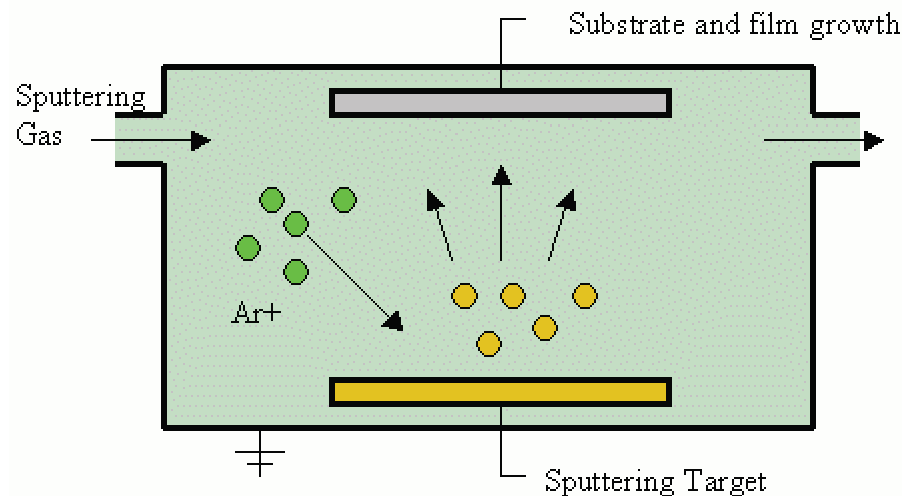

Fig. 2.3 Sputtering process

Before starting the sputtering process, the coating chamber has to be evacuated to a good vacuum, to minimize the influence of residual gases and to increase the mean free path, as measure for impact ionization (Townsend regime). The necessary ions originate from a glow discharge in the working gas (sputtering gas), which in the most cases is argon (inert gas) due to much lower costs in comparison to other noble gases such as krypton or xenon. This glow discharge (self-sustained) is achieved by reaching the breakdown voltage (Paschen law). The evacuated deposition chamber is backfilled with argon to a low pressure regime (<10 Pa) [10]. A usual method, producing plasma from the inert working gas, is to apply a DC (direct current) voltage at the cathode. This imposed potential (U) is up to a few kilovolts (<5000V), whereas the other electrode is grounded. In the classical diode sputter process, the target operates as cathode and the substrate as anode. As a result of this potential, free electrons, which always exist, get accelerated in the electric field. This acceleration causes collisions with the neutral atoms of the working gas.

If their energy is sufficient more electrons are knocked during collisions and the atoms (Ar) become ionized. These electrons get attracted to the anode and the ions are accelerated to the cathode [10].
The striking ions cause a removal of neutral target atoms, emission of secondary electrons and in addition the generation of heat. The secondary electrons are repelled from the cathode, causing further ionization and stabilize the glow discharge. In Fig. 2.4 a schematic illustration of a DC sputtering source in planar configuration with the basic processes during sputtering are shown [10]. These processes range from impact ionization of neutral atoms caused by electrons (a) over ion-induced electron emission on the cathode (b) to electron-induced emission on the anode (c). In (e) reloading processes occur, while (d) shows the aspired emission of neutral particles from the target (sputtering). Simultaneous to the ionisation, procedures such as recombination minimize the ionisation degree. During this recombination or neutralization process, positive and negative particles are combined and build uncharged particles.

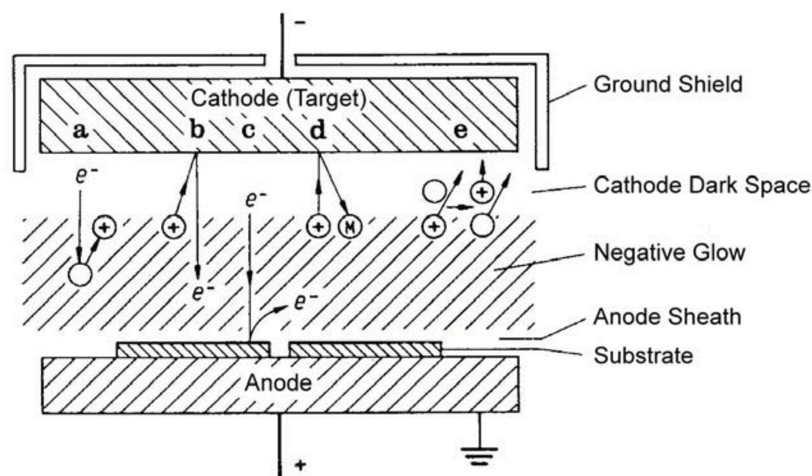

Fig. 2.4 Schematic illustration of the sputtering source in planar configuration; **a** Ionization, **b** Emission of electrons from the target, **c** Emission of electrons from the anode, **d** Emission of neutral particles, **e** Reloading [20]

A main parameter describing the efficiency of the sputter process is the sputter yield. The sputter yield Y is the average number of target atoms, which are emitted per incident ion. Y depends on the target material, the kind, mass and energy of the bombarding ions and their angle of incidence. The sputtering process principally begins at threshold energy E_{thres} of about 10 to 30 eV, which is characteristic for the particular target-ion-combination [8]. As mentioned before, the incident ions interact with the target atoms. The ions loose their energy in form of collision cascades.

Depending on the ion energy and ion mass, three sputtering regimes can be distinguished. These are the “Single-Knock-On-Regime”, the “Linear Collision Cascade” and the “thermal spike regime” [6].

In the depositions carried out in this work, the “Linear Collision Cascade” is predominant. The linear collision cascade regime (Fig. 2.5) happens at higher energy, typically a few 100 eV, than the single knock-on [21].

Each collision involves a moving particle and a stationary particle. If the collision exceeds a certain threshold energy, target atoms can be expelled, or sputtered from the target. This is related to the binding energy of the atoms to the surface. In this manner, higher energy ions can sputter more than a single atom [21].

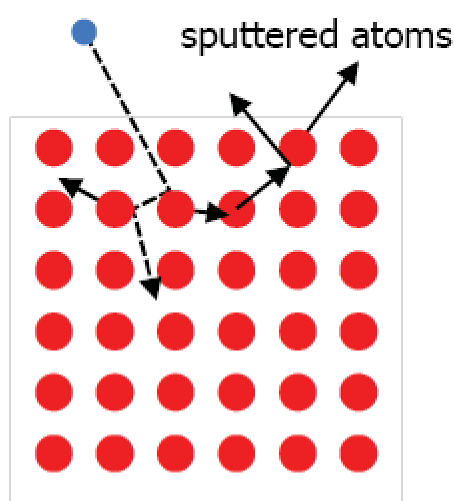

Fig. 2.5 “Linear Collision Cascade” regime

On principle in planar cathode-anode discharges a large amount of electrons are not used for the glow discharge (low efficiency). These electrons are leaving the plasma without energy transfer and, are accelerated towards the anode (substrate), resulting in substrate heating [13].

A magnetron sputtering source addresses the electron problem by placing magnets behind, and sometimes, at the sides of the target (cathode). Within this configuration the chamber wall functions as anode. These magnets cause an increase of the ionization rate by the emitted secondary electrons. In the generated magnetic field, the electrons become captured on cycloidal paths and gyrate over the target surface (Fig. 2.6) [14]. The extension of the electron path, related to the geometric dimensions of the electrodes, results in an extended mean free path [15]. Through the longer dwell time in the gas, the electrons have a higher collision probability and therefore also higher ionisation probability.

As a result the igniting of the plasma occurs at much lower pressures than in conventional sputtering processes [22] and a larger fraction of ions can be extracted from the discharge. Thus, higher film growth rates can be achieved. The sputtered material has minor collisions on the way to the substrate and therefore also the kinetic energy of the impinging particles is higher. Additionally the thermal load of the substrate is reduced by keeping away the electrons.
Until now it was assumed that the substrate is grounded. But it is possible to isolate the substrate against ground and a small voltage against plasma can be applied. Mostly a negative potential (bias voltage, -50 to -500V) is used, which results in an ion bombardment of the substrate. This bombardment of the growing film removes loosely bonded particles (e.g. impurities) and increases the ad-atom mobility [13], thus, serving as a substitute for temperature.

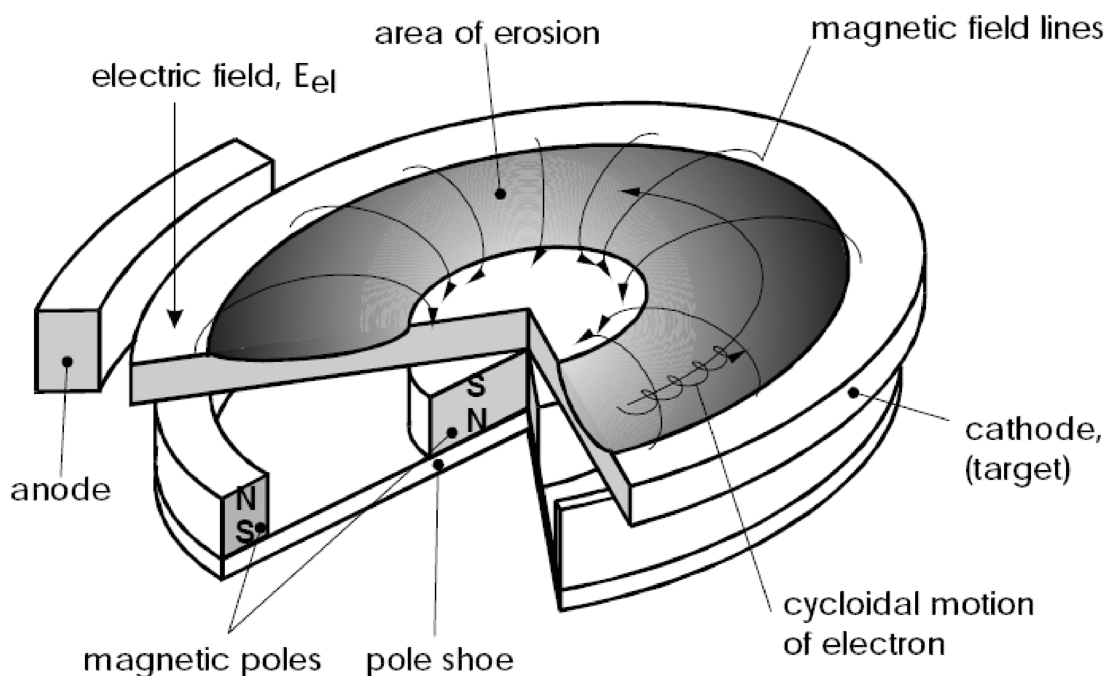

Fig. 2.6 Planar magnetron configuration [14]

The intensity of the ion flux to the growing film can additionally be increased by using unbalanced magnetrons. With the unbalanced magnetic arrangement it is possible to extent the plasma towards the substrate. This can be achieved by using different field strength couplings, resulting in magnetic field lines where uncoupled field lines extend into the chamber. Some of the magnetic field lines run toward substrate and fast secondary electrons that escape from the cathode follow them and undergo ionizing collisions with gas atoms [14]. As a result the plasma expands away from the target surface. The escaping electrons are confined from the magnetic field and determine the number of ions formed, which can be utilized at the substrate.

Typical hard coatings are nitrides or carbonitrides. Therefore sputter deposition of such compounds can be achieved by chemical reactions between the metallic target atoms (e.g. Al, Cr) and a reactive gas (e.g. N_2) introduced into the deposition chamber. At least one component of the finished coating comes from the gas phase.
The reaction, to form the compound, is prone to happen on the substrate, but in most cases on the target too. Rarely it occurs in the gas phase, if the working pressure is low enough. The compound formation on the target is called “poisoning” [23].
If the target is covered with such a compound film, sputtering of this compound instead of the original target material occurs. As consequence the discharge conditions change significantly and of course the deposition process too [14]. This poisoning results commonly in a considerable decrease of sputter yield and sputter rate [23]. Therefore, when sputtering from metal targets, the reactive gas is supplied near to the substrate to initiate there the chemical reaction [13]. Additionally the reactive partial pressure should be kept at low value. Furthermore, the target poisoning can be reduced by using the argon gas fraction to “clean” the target surface from the compound product.
Generally with DC discharge methods only sputtering of conductive targets (metals) can be carried out. The RF-sputtering technique enables the synthesis of dielectric thin films by connecting the target to alternating voltage (radio frequency) [6, 11, 13].
In the following the advantages and disadvantages of magnetron sputtering are summarized [24].

Advantages of sputter deposition:

- Elements, alloys and compounds can be sputtered and deposited.
- The sputtering target provides a stable, long-living vapour source.
- Reactive deposition can be easily accomplished using reactive gaseous species that are activated in plasma.
- There is comparably little radiant heat in the deposition process.

Disadvantages of sputter deposition:

- Sputtering rates are low compared to rates that can be attained in arc evaporation.
- Most of the energy incident on the target becomes heat, which must be removed.
- In reactive sputter deposition, the gas composition must be carefully controlled to prevent poisoning of the sputter target.

2.4 Cathodic arc evaporation

In arc deposition, the vapour source is the vaporization of the anode or cathode of a low-voltage, high-current electric arc in a good vacuum or low-pressure gas [24]. The most common configuration is the cathodic arc where the evaporation is from an arc that is moving over a solid cathode surface. In the anodic arc configuration, the arc is used to melt the source material that is contained in a crucible. The vaporized material is ionized as it passes through the arc plasma to form charged ions of the film material. That means thermal ionization of atoms occurs in a gaseous environment at high temperatures in the vicinity of the arc spot.
In the arc evaporation process, molten globules (droplets) can be formed and deposited on the substrate. The droplet density is influenced by gas type and pressure, vapour pressure and melting point of the cathode material. These macroparticles can be avoided by using curved magnetic fields to direct plasma to the substrate (e.g. plasma duct in Fig. 2.7) [24]. This plasma duct is used to bend the charged particles out of the line-of-sight of the source, and the macros will deposit on the walls of the duct [9]. As negative consequence by using filters is the decrease of the yield [25]. Another possibility to reduce the droplet formation is to cool the cathode surface as good as possible, for maintaining low temperatures. Fig. 2.7 shows some arc evaporation deposition configurations.

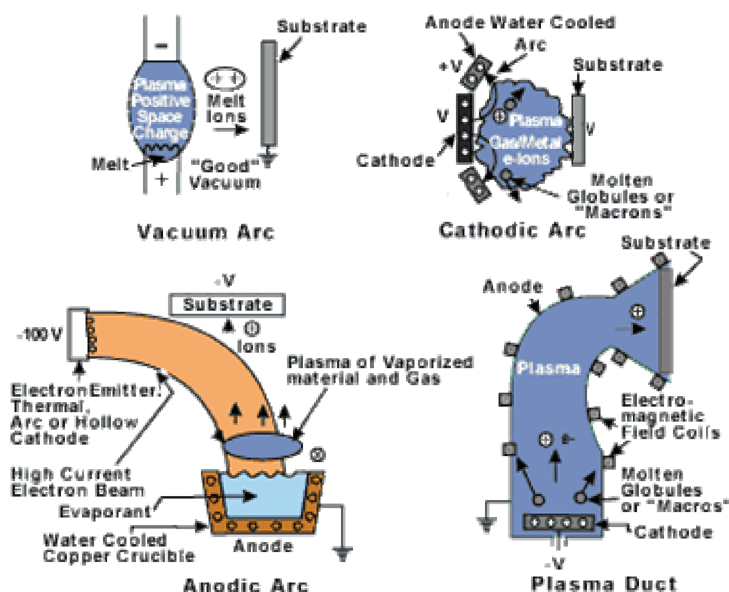

Fig. 2.7 Arc evaporation deposition configurations [24]

In this work the method of cathodic arc evaporation is used for the deposition of the coatings. That means the vaporization occurs at the cathode surface. In this process, an arc (spot) with a diameter of just a few microns runs over the solid target material, causing it to evaporate.

At these cathode spots the current transport is made possible by plasma formation and electron emission. The plasma is formed explosively, caused by high currents and power densities, leading to multiply ionized ions of the cathode material [26]. The main part of the ionization is caused in the cathode spot. Anders et al. published a periodic table of ion charge-state distributions of vacuum arcs for most conductive elements [26].

Because of the high currents and power densities used, the evaporated material is almost totally ionised and forms a high-energy plasma. The current densities within this spot are in the range of about $10^{12}\,Am^{-2}$ and the plasma density reaches $10^{26}\,m^{-3}$ [9]. Further increase in current density results in a splitting of the spot in two or more arcs.

In Fig. 2.8 the arc discharge process, necessary for generating the ion bombardment, is shown. This discharge is a self sustained process, caused by electrons and ions created at the cathode [9]. In case of reactive deposition the arc is sustained additionally by ionized gas atoms caused by collisions.

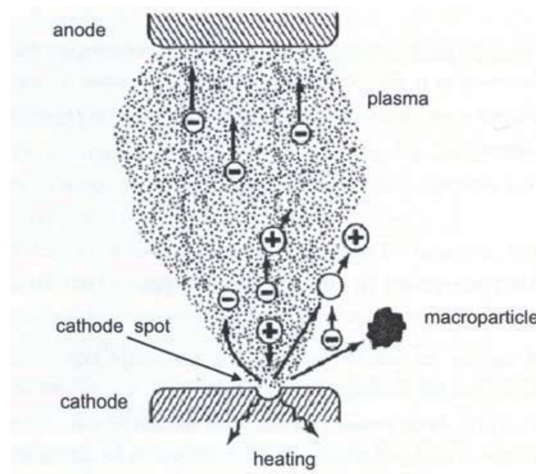

Fig. 2.8 Cathodic arc discharge process [9]

A main disadvantage of cathodic arc evaporation is the formation of droplets, so called macroparticles. These macroparticles are formed as a part of the explosive plasma formation and diminish the quality of the coating. The liquid particles are ejected at small angles with respect to the cathode surface [25]. The number and size of the droplets increases with increasing arc current and cathode surface temperature and is decreased the higher the melting point of cathode material [25]. Münz et al. report about droplet diameters ranging up to 20 µm and a droplet density of $10^{5}\,mm^{-2}$ [27]. These droplets become deposited in the coating and are usually considered to be growth defects [28].

They cause higher surface roughness and detrimentally influence the film properties. Mostly cathodic arc evaporation is carried out in reactive mode. In that case a reactive gas is used to achieve the formation of compounds such as oxides or nitrides. But additionally the reactive gas influences the generation of macroparticles. In fact, with increasing partial pressure of the reactive gas, the number of droplets might decrease [25].

For controlling the arc (spot) movement a magnetic field can be used. These devices controlling the spot splitting, the trajectories and rate of arcs are called “steered arcs” [29]. In the ideal case a diffuse arc (splitting) is moving on the cathode surface.

In the following the advantages and disadvantages of arc evaporation are mentioned.

Advantages of arc evaporation deposition [24]:

- All electrically conductive materials can be vaporized.
- The arc plasma is effective in ionizing the vaporized material as well as reactive gases used in reactive deposition.
- Ions of the film material can be accelerated to a high kinetic energy before being deposited.
- Reactive gases can be activated in the plasma to aid in reactive deposition processes.
- Poisoning the cathodic surface during the reactive arc vapour deposition is much less of a problem than with reactive sputter deposition.

Disadvantages of arc evaporation deposition [24]:

- Only electrically conductive materials can be vaporized.
- Molten globules (macros) ejected from the electrode can be deposited in the film, resulting in growth defects.

3 Coating formation

3.1 General

During PVD coating processes such as magnetron sputtering and arc evaporation, the film material is usually considered to be deposited atom by atom on a substrate by condensation from the vapour to the solid phase. This condensation step is not a random impingement of atoms that stick on the surface at the point of impact. The impinging atoms, which become adatoms, are able to diffuse at the film surface until they get trapped at low-energy lattice sites [8]. The diffusion is mainly established by their energy either provided by substrate temperature or for example by the ion bombardment.

3.2 Nucleation and growth

The formation of a continuous thin layer by deposition of particles from the vapour phase on a solid surface is shown in Fig. 3.1. The adsorbed particles form meta-stable clusters and if these clusters reach a critical size by binding of diffusing atoms or impinging atoms, they become stable and nucleation occurs. The nuclei generated on the substrate surface form the centres of coalescence by surface diffusion of the deposited atoms. Later they form islands aided by the substrate temperature (Fig. 3.1). Ensuring constant temperature on the substrate surface results in a uniform layer growth and a high film density [30].

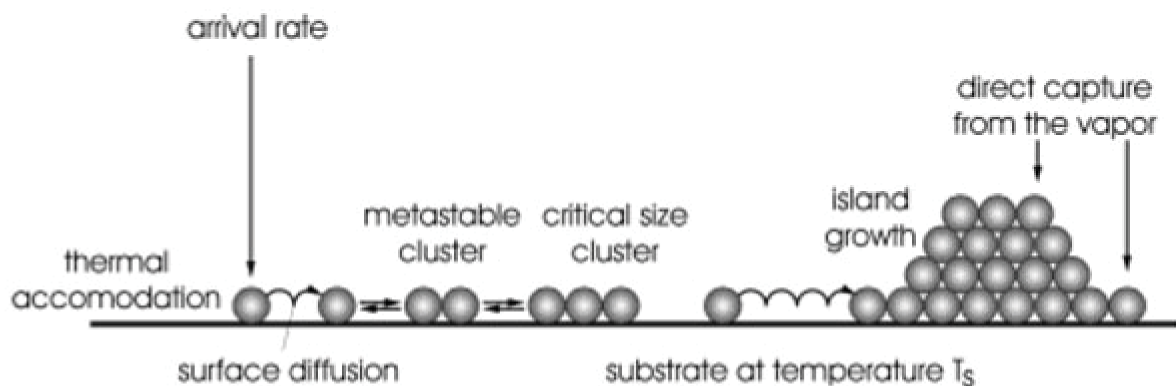

Fig. 3.1 Formation of a thin layer [16]

The critical size of the nuclei and furthermore the beginning of the growth are influenced by the different energies for the adsorption and the bonding energy between two atoms. Depending on these energies three growth modes can be distinguished (Fig. 3.2) [10].

Here, θ means the deposition on the surface in mono layers. If the adsorption energy to the substrate and the diffusivity are high, then layer growth is preferred [16]. This can be seen in figure 3.2.a.

In the Stranski-Krastanov mode or layer + island growth (Fig. 3.2.b), first a layer is formed because of the higher adsorption energy. But then the adatom bonding energy is high compared to the adsorption energy, resulting in island growth on top of the first layer [10]. The third mode describes the island growth or Volmer-Weber mode, in which the adsorption energy is lower than the bonding energy between the atoms (Fig. 3.2.c).

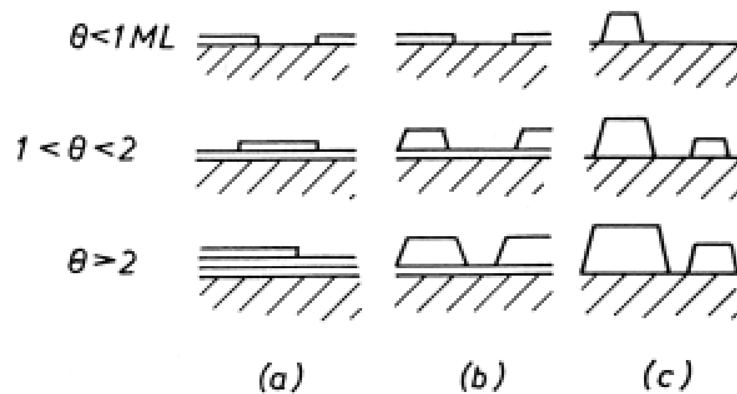

Fig. 3.2 Growth modes; **a** Layer growth (Frank van der Merve mode), **b** Layer+island growth (Stranski-Krastanov mode), **c** Island growth (Volmer-Weber mode) [10]

Until now the nucleation and initial growth have been described. Further growth of the nuclei leads to coalescence of the islands. That means islands with lower energy per atom consume other ones. As a result the system tries to minimize the overall surface and interface energy [16]. Due to the so called atomic shadowing effect (the prevention of filling up all available sites by the atoms arriving with different angle of incidence), a microstructure containing micro channels can evolve depending on the direction of incidence of the incoming atoms, as referred by Deák et al. [31]. These channels get closed by means of diffusion of the particles, depending on the temperature and ion assistance, before a continuous layer is finally formed.

After the substrate is fully covered with a film, the three processes - adsorption, diffusion and desorption - still control further (competitive) growth of the coating. The competitive grain growth depends also on the texture evolution: In TiN (001) oriented islands are lower energy sites and therefore possess lower surface diffusivity in comparison to grains with (111) orientation [16]. The competitive growth is influenced by orientation-dependent adatom transport parameters such as activation barriers for surface diffusion, island edge diffusion, Ehrlich barriers and adatom formation energies and also orientation-dependent step and kink formation energies [32].

Another major parameter affecting the microstructure evolution is the ion bombardment. With the ion bombardment, the ion energy (E_i) and the ion/atom flux ratio is meant [14]. The energy of the impinging ions (E_i) can be adjusted by applying a bias voltage at the substrate and, thus, thermal diffusion limits can be offset [9, 14]. The above mentioned processes and parameters influence the structure of the coating, summarized in the following structure zone models.

3.3 Structure zone models (SZM)

Structure zone models describe the development of grain morphology onto non-epitaxial substrates vs. temperature normalised to the melting temperature T/T_M, also called the homologous temperature. Such SZM's were first proposed by Movchan and Demchishin describing three zones [33]. Fig. 3.3 shows such a diagram after Thornton considering even the effect of Ar pressure, which defines the number and energy of the impinging particles [34].

In ***Zone I*** ($T_S/T_M < 0.3$) the substrate temperature is low and therefore the surface mobility is not sufficient for atoms to move to valleys with lower impingement rate, caused by the shadowing effect. This leads to a porous layer consisting of columnar crystallites with domed heads.

In ***Zone II*** the surface mobility is increased due to higher temperature and therefore voids and valleys can be filled up easier. This results in columnar grains which have rough surfaces. The grain size increases with T_S/T_M. Compared to Zone 1 a denser layer is built.

In ***Zone III***, at the highest substrate temperatures ($T_S/T_M > 0.5$), lattice and grain-boundary diffusion processes dominate, resulting in large equiaxed recrystallized grains and a smoother film surface. The activation energy for grain boundary movement is that of self diffusion in the film.

In ***Zone T*** (named by Thornton), which is often called as the transition region between zones 1 and 2, a dense array of poorly defined fibrous grains, exist [35]. The grains have different sizes in a range broadening with increasing temperature.

Due to higher diffusion the surface is getting smoother, but nevertheless voids exist.

Generally it can be said that with increasing argon pressure the Zone T is shifted to higher temperatures but additionally the Zone T narrows. This is attributed to the collisions between the target atoms, on their way to the substrate, and atoms of the inert gas; because collisions mean a loss of energy and this result in a lower mobility of the impinged atoms on the substrate.

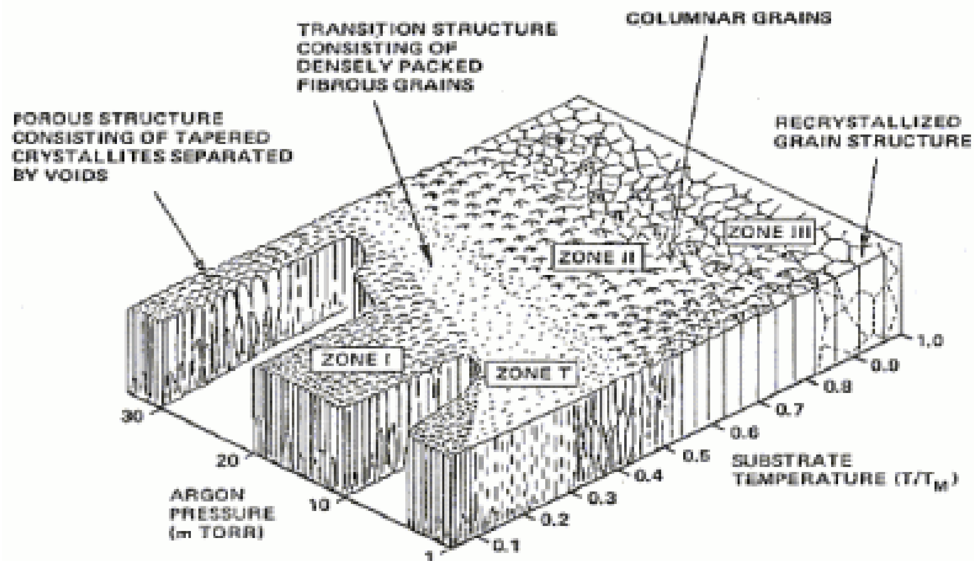

Fig. 3.3 Structure zone model after Thornton [34]

Messier et al. refines the structure model from Thornton and replaces the gas pressure by the bias voltage (Fig. 3.4) [36]. So Messier et al. were able to analyze influences caused by the energy of the impinging particles. This model shows the same structures as Thornton's, but the course of the boundary between Zone T and Zone 1 is inversed. That means that with increasing bias voltage the transition zone between Zone 1 and Zone 2 is widened. A higher bias voltage leads to higher ion energy and therefore the mobility on the surface is increased, resulting in a densification of the film. Further increase of ion bombardment leads to implantation, renucleation, equiaxed grains or elongated grains [16]. Nevertheless defect generation also occurs by increasing the bias voltage.

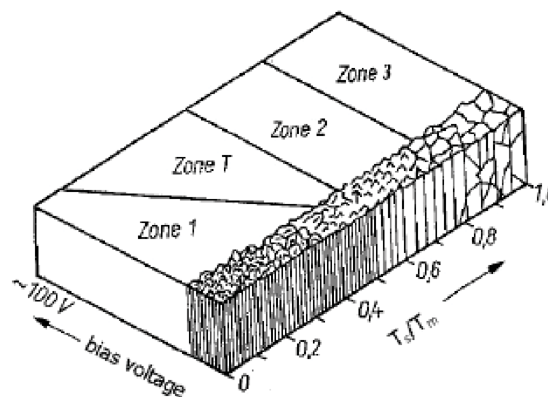

Fig. 3.4 Revised structure zone model after Messier et al. [36]

In general, the grain orientation in polycrystalline films tends to have close packed planes outward. This maximizes atomic density on the initial surface and minimizes surface energy. Therefore fcc metals tend to have a (111) preferred orientation, bcc metals the (110) orientation and hex metals prefer the (0002) orientation [37].

4 Experimental

4.1 Coating synthesis

4.1.1 Deposition plant

The deposition of the coatings was carried out in an industrial-scale RCS (rapid coating system) 900 plant from Oerlikon Balzers Coating, shown in Fig. 4.1, placed at their branch in Kapfenberg.

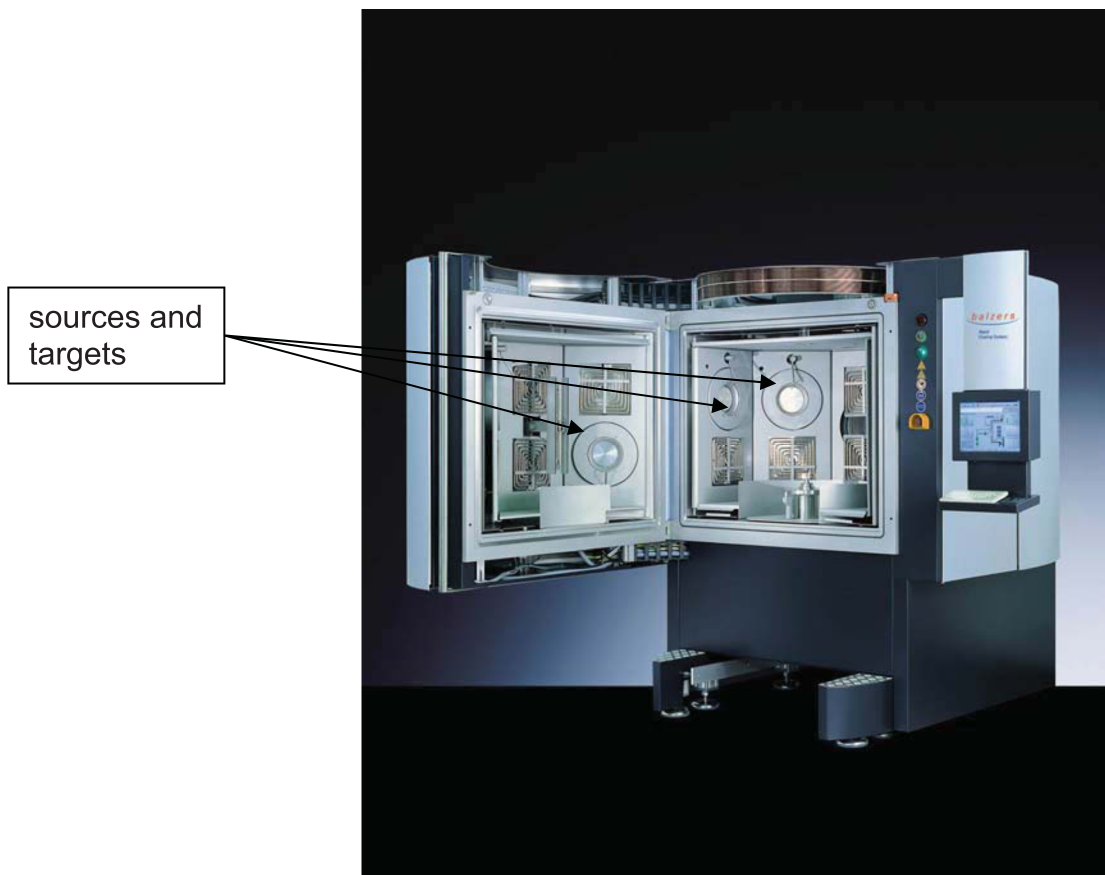

Fig. 4.1 RCS-plant from Oerlikon Balzers, without substrate carrousel

The vacuum chamber has a volume of about $1000\,l$. The device is equipped with six sources positioned on two planes, which can be run in either sputter or cathodic arc mode. In Fig. 4.2 the arrangement of the sources is schematically shown - sources 1, 2 and 5 are on the lower plane and sources 3, 4 and 6 on the upper plane. However, in the current setup, only in the cathodic arc mode all sources can be used.

The magnetron sputter process is just feasible with two sources at a time, due to a limitation of the power supplies. Further details can be found on the Oerlikon Balzers website [38].

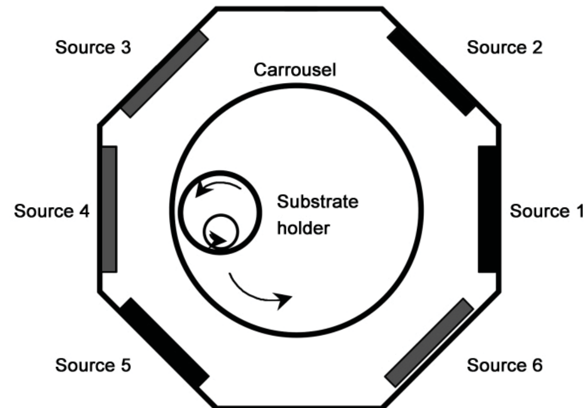

Fig. 4.2 Schematic of the Oerlikon Balzers RCS coating system, including substrate carrousel

During arc evaporation, specific magnetic systems for the most common target materials optimize the target utilization and lower the droplet emission. The various magnetic systems apply different magnetic fields and by that influence the motion and dwell time of the arc spot(s), whereas for sputtering kidney-shaped rotating unbalanced magnetic systems are used as well as a high voltage instead of a high current power supply.
A main advantage of this plant is the simple change of the targets (cathodes) and magnetic systems. In the magnetron sputter mode the magnetic system Mag127 is the current setup, during cathodic arc evaporation Mag10 was used. The substrates were mounted on satellites and these satellite trees are fixed on the carrousel. The carrousel rotates and the trees as well as satellites additionally rotate resulting in a 3-fold rotation (Fig. 4.2). With the help of the so-called Balinit-Editor, the recipes for the deposition procedure can be written. Afterwards the process can be started and runs automatically including cooling and various test procedures (e.g. leak test).

4.1.2 Targets, gases, substrates

The targets have a diameter of 150 mm and have been produced by forging of AlCr powders [39]. This results in a dense matrix [39]. The compositions used range from 25 at% Al over 70 at% to 85 at% Al, while the remaining part is Cr.

For low aluminium content in the target (25 at%), density problems might occur by using the forging technique and, thus, the targets were reinforced by a pure aluminium backing plate. To get an Al-Cr-N film, the reactive nitrogen gas is introduced in the vacuum chamber during deposition. Additionally, Argon (Ar) was used as working gas only for sputtering. Inert Ar was also utilized for substrate heating and ion etching prior to deposition.
In this work, different sizes of silicon samples as well as cemented carbide cutting inserts (grade 10), high speed steel coupons (HSS, DIN 1.3343) and tempered steel samples (QRS, 90MnCrV 8, DIN 1.2842) served as substrate. The HSS discs (∅ 40mm) were ground and polished to a 1 µm finish. From the coated HSS substrates the coating thickness (section 4.2.1), the hardness (section 4.2.6) and the crystallographic structure (section 4.2.4) of the film was determined. QRS samples were coated in each deposition run for ex-situ determination of the deposition temperature (see below). The silicon samples of the dimensions 7 x 20 mm were cut from a silicon 525 µm double side polished (100) wafer, while the 20 x 20 mm samples had a thickness of 315 and were just polished on one side. With the smaller silicon samples, biaxial stress temperature measurements were carried out (see section 4.2.5).

4.1.3 Deposition procedure

Prior to deposition, the specimens are mounted on the substrate holder, after cleaning with acetone and ethanol in an ultrasonic bath for ten minutes each. The substrate holder is mounted on the carrousel in the plane of the lower sources, and for both cathodic arc evaporation and magnetron sputtering the carrousel is stopped after heating and etching and kept stationary during the deposition process for comparative reasons with the substrates facing source 1 at a distance of approximately 21 cm (Fig. 4.3).

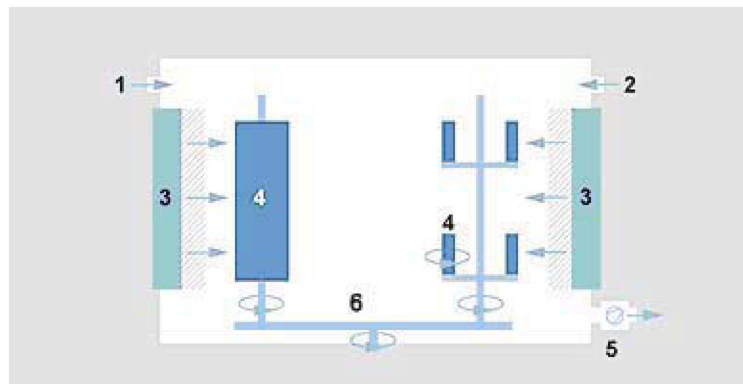

Fig. 4.3 Deposition chamber. **1** Argon, **2** Reactive gas, **3** Planar magnetron source (coating material) or arc evaporation source (coating material and backing plate), **4** Components, **5** Vacuum pump, **6** Carrousel [38]

With this industrial scale deposition plant it is possible to run the process automatically. In this case it is necessary to write the recipe for the wanted deposition process. To programme the recipe, the above mentioned “Balinit Editor” is used. The recipe includes the sequences: pumping, heating, etching and coating (Fig. 4.4).

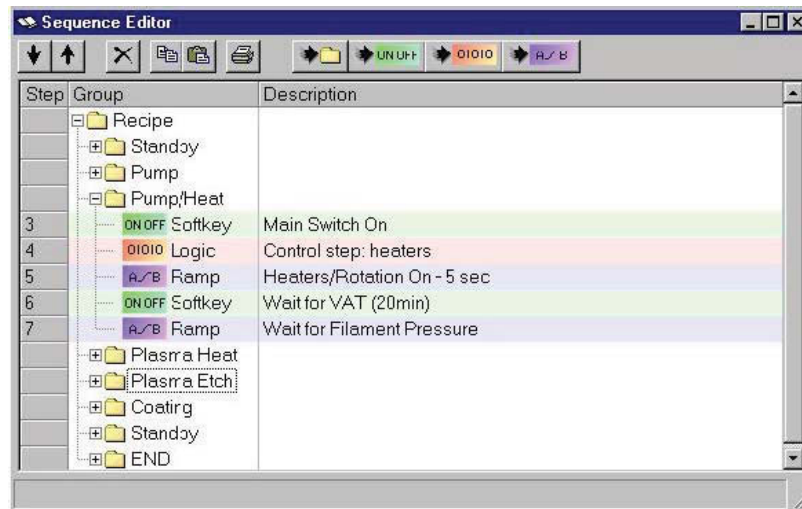

Fig. 4.4 „Balinit Editor“

In the pumping sequence the chamber is evacuated with the help of a combination of rotary vane pump (fore pump), roots pump and a turbo molecular pump to a base pressure of $5x10^{-6} mbar$. Then the substrates were rapidly heated by means of radiation heaters and an electron bombardment, originating from a secondary gas discharge, sustained by an additional ionization chamber [40]. The next step is the plasma etching process, where the discharge burns on a secondary anode. Here, argon ions provided by the above mentioned gas discharge get attracted to the substrate holder by a high bias voltage (-200V). Due to the high ion energy, substrate surface etching occurs. Until the end of the etching sequence the carrousel is rotating. This etching sequence takes about 25 minutes. Afterwards the actual coating procedure is initialized. Radiation heaters at the chamber walls keep the temperature constant at 500°C during etching and deposition. These radiation heaters are controlled by thermocouples, mounted in line-of-sight of the substrate carrousel. Additionally the deposition temperature was ex-situ determined by the defined drop in hardness (HRC) of the tempered steel samples (QRS). All coatings accomplished in this work are deposited in the stationary mode by cathodic arc evaporation and magnetron sputtering. Detailed process and deposition conditions for both cathodic arc evaporation and magnetron sputtering will be described in the following sections 4.1.4 and 4.1.5.

4.1.4 Magnetron sputtered coatings

The first coating runs were used to determine global settings for the intended comparison. This includes the choice of the most efficient sputter power, since the sputter yield (number of sputtered atoms per incident ion) and rate depends on the supplied power. At the beginning a sputter power of 6 kW (39 Wcm^{-2}) was selected. However, as consequence of the high current (14 A), the cables as well as the target itself were at their thermal limit. Therefore the sputter power was reduced to 4 kW (26 Wcm^{-2}). Another global adjustment was the nitrogen partial pressure. During reactive sputtering the total pressure was held constant at 1 Pa. The nitrogen fraction was first varied from 0% to 100% to get information about the interplay between deposition rate and stoichiometry. Finally the nitrogen partial pressure was set to 25% (to minimize target poisoning, while still retaining the $Al_{1-x}Cr_xN$ stoichiometry) and back-filled with argon to the constant total pressure as regulated by a capacitive gauge.
In Table 4.1 the parameters which are constant during deposition are summarized.

Table 4.1 Constant parameters during magnetron sputtering

total pressure ($Ar+N_2$) [Pa]	Sputter power [kW]	Temperature [°C]	Distance substrate-target [mm]	stationary
1 (25% N_2)	4	500	250	yes

To the variable parameters belong the target composition (see section 4.1.2), the bias voltage and duration of the deposition. The depositions were carried out applying a negative bias voltage of -40 V over -100 V to -150 V, which leads to attraction of ions to the substrate. With increasing negative bias voltage the ion energy is increased and as consequence the growth is influenced [9]. The deposition time was varied depending on the target composition and the desired thickness between 40 and 200 minutes. After the deposition process, the source is switched off automatically and the system cools down using helium (He) on account of its high heat capacity. In Table 4.2 the parameters for the various sputtered coatings are listed.

Table 4.2 Magnetron sputtered coatings

Target [Al/Cr]	Bias voltage [V]	coating time [min]
25/75	-40, -100, -150	40
		200
70/30	-40, -100, -150	40
		200
85/15	-40, -100, -150	40
		200
	-100, -150	60
		110

4.1.5 Arc evaporated coatings

For the deposition of arc evaporated coatings pre-established parameters have been used. This includes a nitrogen pressure of 3.5 Pa and an arc current of 140A, which is applied to the source, resulting alongside with Mag10 in good arc dispersion. The deposition temperature and the distance between substrate and target is the same as for magnetron sputtering. In Table 4.3 the constant parameters during deposition are listed.

Table 4.3 Constant parameters during arc evaporation

total pressure N_2 [Pa]	Arc current [A]	Temperature [°C]	Distance substrate-target [mm]	stationary
3.5	140	500	250	yes

For the arc evaporated coatings, the same target compositions were used as for magnetron sputtering. The bias voltage was also varied from -40V to -150V. Due to the higher deposition rates in the arc evaporation process, the coating time ranges only from 5 minutes up to 40 minutes. In Table 4.4 all realized arc evaporated depositions are summarized.

Table 4.4 Arc evaporated coatings

Target [Al/Cr]	Bias voltage [V]	coating time [min]
25/75	-40	30
	-100	30
	-150	15
70/30	-40	15, 40
	-100	5, 10, 15, 30
	-150	5, 15
85/15	-40	15, 30
	-100	5, 30
	-150	15, 40

4.2 Coating analysis techniques

4.2.1 Coating thickness

The coating thickness (t_c) was measured using the ball cratering method, schematically shown in Fig. 4.5. With this method a film thickness above 1 µm can be determined. The specimen tested is fixed on a table inclined in an angle of 60°. For the abrasion of the coating material, a steel ball with a diameter (D) of 25 mm, spread with a diamond paste of 1 µm, is used. This steel ball (and abrasive particles) grinds a hole in the coating by rotational motion. The resulting crater has the shape of a spherical calotte.

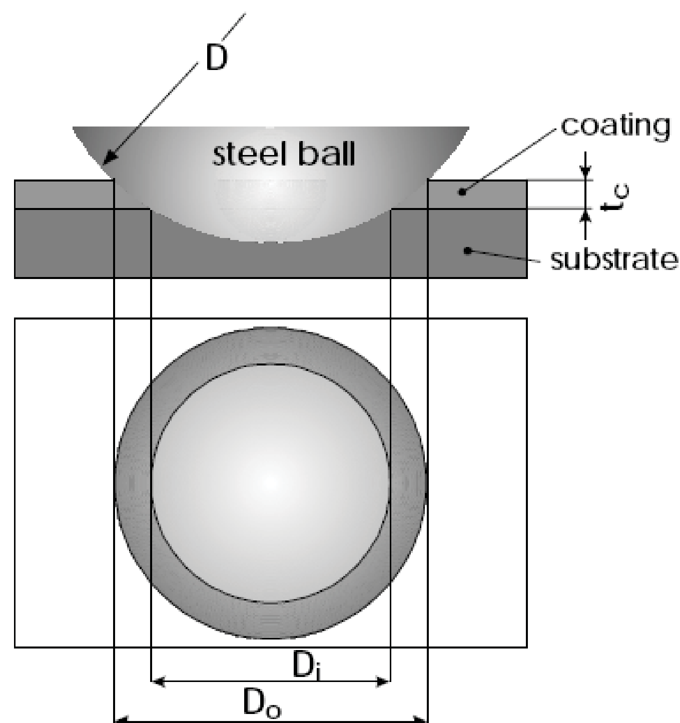

Fig. 4.5 Ball cratering method [14, 41]

After the grinding process, the calotte has to be cleaned with alcohol. With the help of an optical microscope the inner (D_i) and the outer diameter (D_o) of the calotte can be measured. The coating thickness (t_c) can then calculated by using these diameters and the diameter of the steel ball, following eq. (7).

$$t_c = \frac{D_o^2 - D_i^2}{4 \cdot D} \tag{7}$$

4.2.2 Scanning electron microscopy (SEM)

With a scanning electron microscope it is possible to scan a surface by means of an electron beam. In contrast to the magnification of a light optical microscope (max. 2,000:1), magnifications up to 300,000 can be achieved with the SEM, due to the shorter de Broglie wavelength of the electrons which are emitted from a cathode. These electrons get accelerated by means of a strong electromagnetic field (up to 40 keV) and through several electromagnetic lenses the diameter of the electron beam is reduced down to 3 nm. This electron beam is scanning over the sample surface line by line and thereby secondary electrons are released. The obtained signal becomes amplified and then monitored. The resolution is in the range of a few nanometres [42].

The scanning electron microscope was used to evaluate the morphology of the coatings. SEM was carried out at fracture cross sections and surfaces of arc evaporated Al-Cr-N coatings deposited on silicon substrates. The scanning electron microscope images were taken with a Zeiss Evo 50. This SEM is equipped with a secondary electron (SE) detector and a backscattered electron detector. For these investigations the SE-detector was used.

4.2.3 Optical profilometry (white light interferometer)

With the white light interferometer it is possible to characterize the surface topography. That means characteristic values such as roughness (R_a, R_z or R_t) and wear rates [16, 43]. In Fig. 4.6 the principle behind “Scanning White Light Interferometry” is shown.

The measurements were carried out on a Veeco Wyko NT1000 optical profiler. During the measurement the surface is illuminated with white light and scanned, whereby the objective is moved a defined distance in height. The light reflected by the object surface interferes at fulfilled interference conditions with the light of a reference surface. During the vertical movement of the objective, different points of surface are in the focus. By determination the points of maximum modulating and by knowledge of the objective position the surface profile is reconstructed.

The vertical measurement range is restricted to 0.1nm up to 1mm, a lateral resolution of about 50nm and the vertical resolution is limited with 3nm. Further limitations of the optical profilometer are given in [16].

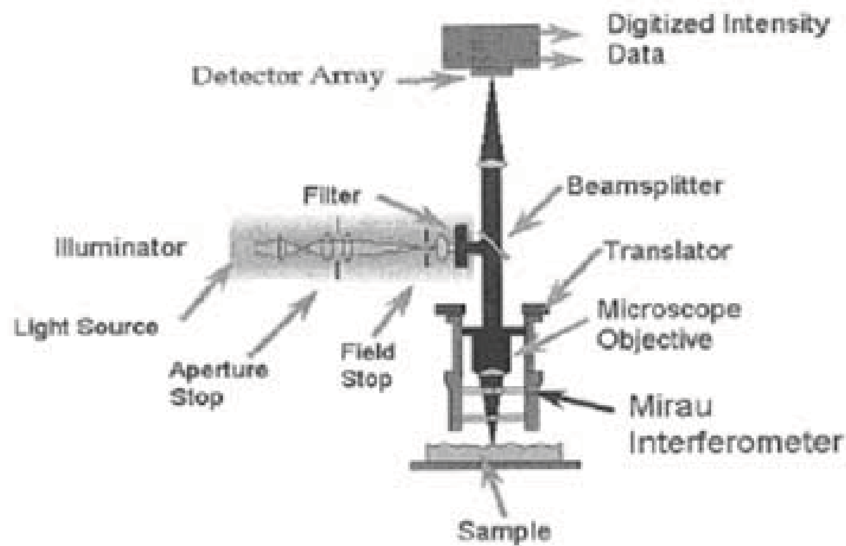

Fig. 4.6 White Light Interferometer [16]

4.2.4 X-Ray-Diffraction (XRD)

For the determination of the crystallographic structure of the coatings a Siemens D500 diffractometer is used. The principle of the plant is based on the physical effect of the Röntgen diffraction at crystal structures [44]. The sample is irradiated with a confocal X-ray beam of certain wavelength (CuK_α) at an angle θ to the sample surface and the diffracted beam intensity is detected at an angle 2θ with respect to the incident beam. This is the so called θ-2θ scan (Bragg/Brentano) [44, 45]. To avoid the K_β-peak (already minimized by a Ni foil in front of the source) and the fluorescence radiation, a secondary monochromator (graphite) is installed in front of the detector.
Only if the Bragg condition is fulfilled (eq. 8), the incident X-ray at the sample is reflected and detected (Fig. 4.7) [46].

$$n \cdot \lambda = 2 \cdot d \cdot \sin\theta \tag{8}$$

In eq. (8) λ is the wavelength, d is the distance between two lattice plains and θ is the angle of incidence and reflection.
For each value of d a reflection occurs and can be seen as a peak on the recorded pattern. Comparing the measured pattern of the sample with well known crystal structures, the crystal structure of the specimen can be determined [47].

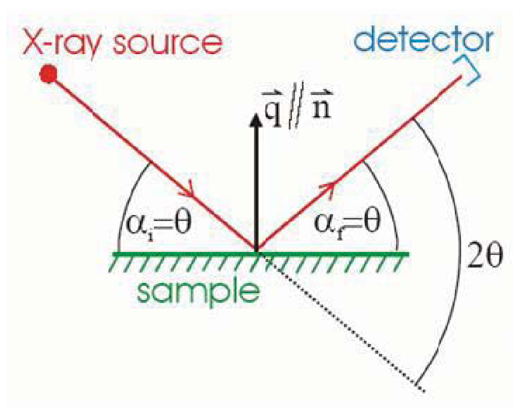

Fig. 4.7 Principle of X-ray diffraction [46]

In Table 4.5 the parameters for the XRD measurements are summarized.

Table 4. 5 Diffraction parameters

Wavelength Cu-Kα1 [nm]	Kβ-filter	Tube current [mA]	Voltage [kV]	2θ angular speed [°·min-1]	Tube aperture [°]	Detector aperture [°]
0.154056	Ni	40	40	0.02	1	0.15

To get more detailed information about texture evolution in the Al-Cr-N coatings, texture coefficient calculations were performed using the Harris analysis [48]. This calculation is based on the comparison of the peak intensities of each diffracting plane of the deposited coating with the standard intensity of a randomly oriented sample. As a result the orientation with the highest texture coefficient seems to be the preferred one.

Rietveld refinement

Rietveld refinement was carried at the Institute of Mineralogy of the University of Innsbruck, to determine the phase composition of the Al-Cr-N thin films synthesized by cathodic arc evaporation and magnetron sputter method. The principle of the Rietveld method is to minimize the difference between a calculated profile and the measured data from XRD by means of least-square method. Parameters necessary for the Rietveld refinement are the crystallite size, the strain of the lattice and the lattice parameters. Detailed description about Rietveld refinement is given in [49]. The Rietveld software used for the analysis of the phase mixture is called TOPAS, developed by the Bruker AXS Company. Further details about the software can be found on their website [50].

4.2.5 Biaxial stress temperature measurements (BSTM)

To determine the residual stresses in coatings, biaxial stress temperature measurements were carried out. The residual stresses can be divided into the intrinsic and extrinsic stresses [51]. The intrinsic part is caused by the deposition process itself, influenced by the nucleation, ion energy and ion/atom arrival rate. Extrinsic or thermal stresses are caused by a different thermal expansion coefficient of substrate and coating.
In Fig. 4.8 the substrate-coating composite is shown [14]. If the substrate is coated just on one side, the whole composite is bent. Here, l_x and l_y are the dimensions of the specimen, t_c and t_s are the thickness of the coating and the substrate. If the curvature is measured, the biaxial stress (occurring in x- and y-direction) can be calculated.

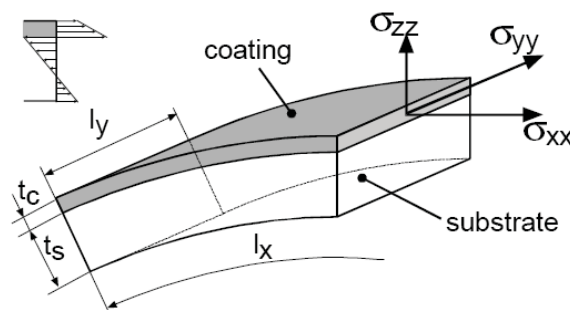

Fig. 4.8 Bent coating substrate composite [14]

As substrate silicon with the dimensions 7x20x0.5 mm was used. Due to the larger length the curvature is more pronounced in the x-direction and therefore the biaxial stress state can be assumed as uniaxial stress state.
After deposition the specimens are placed with the coated face down on a heating plate, which can be stepwise (25 K) heated up to 700°C. To avoid contact with air the chamber is evacuated up to 0.1 mPa. A complete measurement includes stepwise heating up to 700°C and cooling down to room temperature. The heating rate was adjusted with 5 K/min.
To determine the bending, two parallel laser beams with the distance d_0 hit on the polished backside of the sample. In Fig. 4.9 it can be seen that h_1 is the distance between mirror and heating plate and h_2 is the spacing between the mirror and the measuring plate (h_1 = 1434mm, h_2 = 1334mm). The reflected beams meet a mirror, placed below the laser, under a certain angle and these beams are reflected again to the measuring plate (Fig. 4.9) [14, 51].

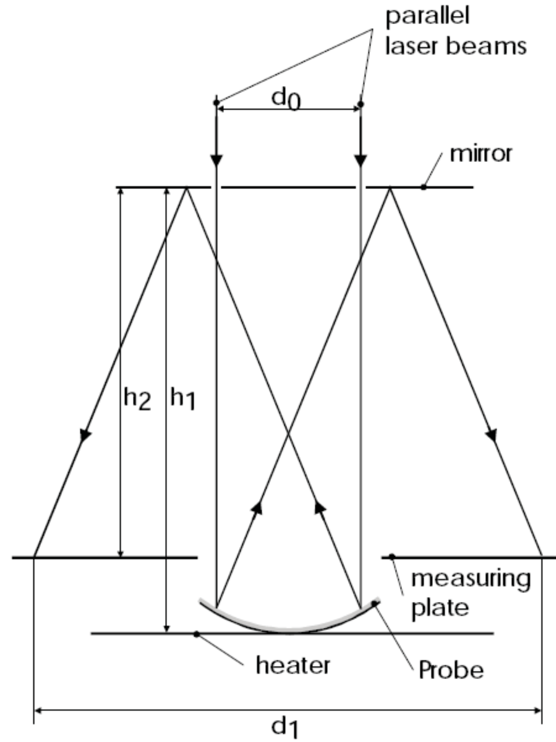

Fig. 4.9 Principle of the stress measurement [14]

Now the distance between the two points (d_1) can be measured and with that, the curvature (r) is evaluated using eq. (9) [51]. If the curvature of the specimen is convex, that means the reflected beams do not cross, then the distance has to be set as negative value.

$$r = \frac{2 \cdot (h_1 + h_2) \cdot d_0}{d_0 - d_1} \tag{9}$$

The stress in the coating (σ_f) is calculated using the modified Stoney formula (eq. 10) [52]. In this equation, E_s is the elastic modulus of the substrate; ν_s is the Poisson's ratio of the substrate and r_0 is the curvature prior to deposition. As mentioned before, t_c and t_s are the thickness of the coating and the substrate. The values for E_s and ν_s are 159.6 GPa and 0.228 respectively, given by Janssen et al. [53].

$$\sigma_f = \frac{E_s}{1-\nu_s} \cdot \frac{t_s^{\,2}}{6 \cdot t_c} \cdot \left(\frac{1}{r} - \frac{1}{r_0} \right) \tag{10}$$

Additionally to the stresses, it is possible to calculate the linear thermal expansion coefficient of the coating from the ideally linear thermo-elastic part of the BSTM curves by inserting in eq. (11) [54].

$$\frac{d\sigma}{dT} = \frac{E_C}{1-\nu_C}\left(\alpha_S - \alpha_C\right) \tag{11}$$

In this equation, E_C is the elastic modulus of the coating, ν_C is the Poisson's ratio and α_S is the linear thermal expansion coefficient of the silicon substrate ($\alpha_S = 3.55 \times 10^{-6} K^{-1}$) [55]. T_0 and T_C are the temperatures on the linear part of the stress-temperature curve. $\Delta\sigma$ is the difference in stress corresponding to the stress values of these two temperatures. Detailed information about the equipment is given in [51].

4.2.6 Nanoindentation

To get information about mechanical properties, such as hardness and modulus, nanoindentation was conducted. The determination of hardness and modulus was done using a Fischerscope H100 [56]. This device continuously measures indentation depth during a step wise in/decreasing load. Fig. 4.10 shows a complete curve, consisting of a loading and unloading cycle, which is similar to those investigated in this thesis.

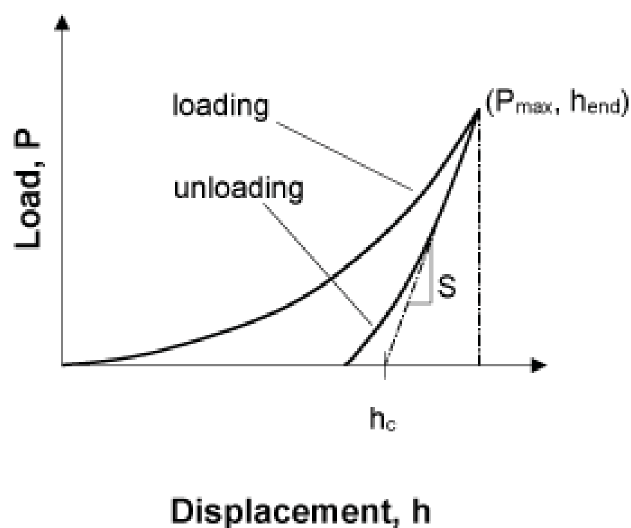

Fig. 4.10 Load indentation curve

The imprints are created using a Vickers indenter, that means a diamond with quadratic base and an angle of 136° between the lateral surfaces is pressed into the surface.

The measurement method used for analysing the coatings in this thesis is the Universal Plastic hardness HU_{pl} according to Fischer [56]. In conventional methods the hardness value includes the plastic and elastic deformation. But the Universal Plastic hardness excludes the elastic part from the hardness value, by calculating the elastic part from the slope of the unloading curve.

In this work, the hardness measurements were accomplished at constant indentation depth. That means after a fixed period (in this case 20 seconds) the maximum indentation depth h_{end} is reached and it takes the same time to unload the specimen. The maximum load P_{max} can be taken directly from the measurement. In the unloading cycle a tangent is constructed to the point of maximum load. This line describes the part of elastic deformation. Reducing the load to zero leads to recover of the elastic deformation. The tangent intersects the displacement axis and generates the value h_c representing the plastic deformation under the maximum load (Fig. 4.10). As a result the Universal Plastic hardness HU_{pl} can be calculated as shown in eq. (12).

$$HU_{pl} = \frac{P_{\max}}{26.43 \cdot h_c^{\ 2}} \qquad (12)$$

The factor 26.43 arises from the relation between the projected area of contact and the depth of the imprint, by using a Vickers indenter [57].

The hardness value and the elastic modulus are automatically calculated by the software WIN-HCU. Generally with the Fischerscope the obtained elastic modulus is underestimated. The hardness value for one sample is calculated by measuring 10 loading-unloading cycles. From these measured values the mean value is formed.

If one of the measured values is failed for example by vibrations shown as tines in the load-depth plot, this value has to be deleted.

To minimize the influence of the substrate, the indentation depth should be lower than the tenth part of the coating thickness. To fulfil this requirement, a constant indentation depth of 0.5 µm was used for all measurements. This kind of measuring allows the qualitative comparison of the obtained hardness values.

Prior to measurements the samples were diamond polished to a 1 µm finish, to achieve moderate roughness. Additionally the shape of the Vickers tip was calibrated on a single crystalline sapphire plate according to Fischer [40].

In contrast to the common Oliver and Pharr method it utilizes the approach of a depth independent Martens hardness (eq. 13),

$$H_M = \frac{P_{\max}}{A_{\max}} \tag{13}$$

which is not always appropriate especially for thin hard coatings [58].
Drawbacks of the device are the instrument frame compliance, the initial penetration and the indenter area function [57]. As consequence of these drawbacks considerable fluctuations of the measured hardness values have been described in literature [57].

4.3 Plasma investigations

4.3.1 Planar probe measurement

To gain information about the parameters influencing the film growth and structure evolution, plasma measurements were carried out. A way to determine plasma parameters such as the floating and plasma potential, ion and electron density is to record a voltage-current characteristics of a conductive probe in the plasma.
For the measurements of the ion dominated parameters, five probes with a diameter of 21 mm were used. These probes were arranged vertically one above the other with a distance of 50 mm in each case (Fig. 4.11). The distance between the probes, fitted on the carrousel, and the target was 210 mm.

Fig. 4.11 Ion probe arrangement

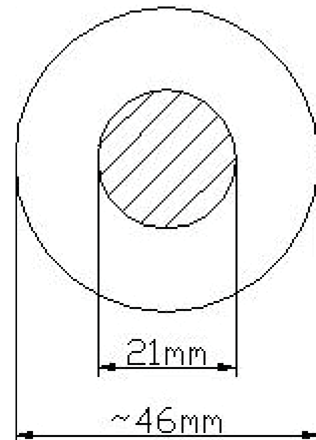

Fig. 4.12 Schematic view of a probe

As mentioned before the probe diameter is 21 mm, but as can be seen from Fig. 4.12 the total diameter is 46 mm. The hatched area (~346 mm^2) is the actual probe surface, which is surrounded by an outer ring. This guard ring, biased to the same potential as the probe throughout the discharge, is used to assure that edge effects are properly suppressed [59]. Booth et al. proposed to design the guard ring to extend the probe sheath sideways at least as far as the maximum sheath thickness [59]. As consequence of the correct design, a complete ion current saturation is achieved at large bias voltages.

In Fig. 4.13 the circuit diagram of the planar probe measurements is shown. To measure the floating potential and the current a voltmeter was used. These parameters were measured for different values of bias voltage, nitrogen and argon pressure, sputter power (magnetron sputtering) and arc current (arc evaporation).

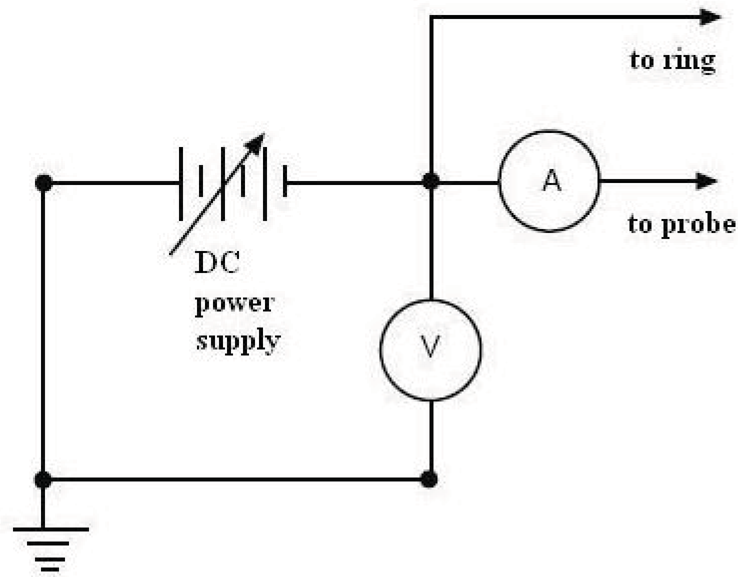

Fig. 4.13 Circuit diagram of plasma measurements

With the measured values of the floating potential and the ion saturation current, different characteristics such as ion flux density I_0, incorporation rate J and the ion assistance α can be calculated.

The ion flux density I_0 is the number of ions impinging on the target surface per second in accordance with Mayrhofer et al. (eq. 14) [16].

$$I_0 = \frac{I_{pr}}{e \cdot A_{pr}} \tag{14}$$

Here, I_{pr} is the current measured on the probe and A_{pr} is the area of the probe. For the determination of the ion flux density I_0, a few assumptions had to be taken. Within these measurements only single charged ions are taken into consideration. However, especially during cathodic arc evaporation multiple charged ions occur [26], resulting in a higher current per impinging ion [9, 25] and, thus, an overestimation of I_0. Furthermore, the emission of secondary electrons is neglected, which might occur upon ion impact reducing the measured current. This effect should, however, be rather constant at the fixed measuring potential.

To get information about the number of atoms/ions deposited on the substrate per second, the incorporation rate $J_{Al\&Cr}$ has to be calculated (eq. 15) [16].

$$J_{Al\&Cr} = \frac{t_c \cdot N_A \cdot \rho}{A_M \cdot d_t} \tag{15}$$

In this equation t_c is the coating thickness, N_A is the Avogadro constant and A_M is the atomic mass and d_t is the deposition time. ρ stands for the ideal coating density calculated for Al-Cr-N (B1 and B4 structure), but this assumption excludes underdense regions such as grain boundaries which exist in most materials (with the exception of single crystals).

Derived from the ion flux density I_0 and the incorporation rate $J_{Al\&Cr}$ the ion assistance can be evaluated. The ion assistance α is the ratio of the ion flux density to the incorporation rate (eq. 16).

$$\alpha = \frac{I_0}{J_{Al\&Cr}} \tag{16}$$

The ion assistance is also an element of uncertainty. For the precise determination of α a positive bias voltage would have been necessary to repel ionized particles from the substrate in order to measure the contribution of the sole atomic (neutral) flux to the growth. However, with the used coating equipment only negative bias can be applied.

Additionally the electron temperature T_e can be calculated from the already measured floating potential V_{fl}, by means of eq. (5), shown in section 2.2.1. Furthermore, the ion density n_i can be determined by using eq. (6), shown in section 2.2.1.

5 Results and discussion

5.1 Coating synthesis

Coating composition measurements were not conducted within this thesis, but values were found in literature for comparable synthesis conditions. Franz et al. determined the chemical composition by electron probe microanalysis (EPMA) [60]. These measurements have shown that the coatings are stoichiometric concerning nitrogen content. The target compositions are nearly reflected by the metal ratio (Al/Cr) in the coatings, only a slight Al deficiency was detected. Comparing the Al loss (coating/target) for magnetron sputtered and arc evaporated films resulted in higher values for the latter one (~4%). These results are in good agreement with earlier measurements, given in [4].

5.1.1 Thickness and growth rate

The thickness of the coatings deposited ranges from about 1μm up to 13μm depending on the coating time. The deposition times used in this work range from 5 to 40 minutes for arc evaporation and in the case of magnetron sputtering from 40 up to 200 minutes. For the determination of the thickness the ball cratering method was used, as described in the experimental part (section 4.2.1). In Fig. 5.1, an abrasion crater caused by a steel ball is shown. This abrasion crater was created on a QRS sample coated with a film sputtered from the 25Al/75Cr target. The gradual transition form coating to substrate without spallation seen in the abrasion crater in Fig. 5.1 indicates the good adhesion between the substrate and the coating.

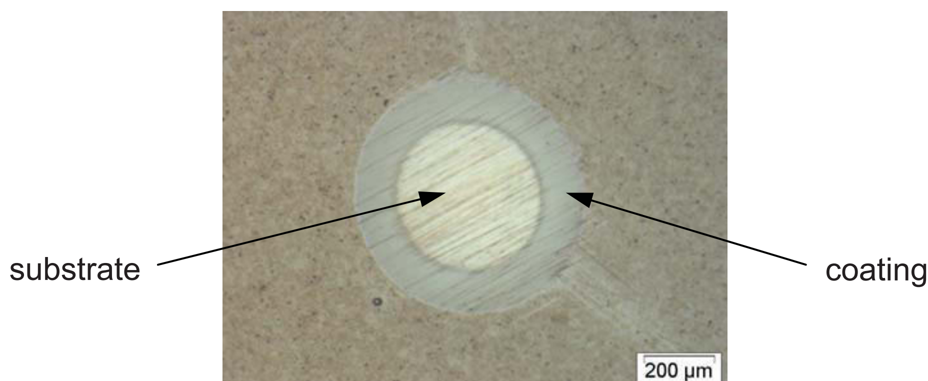

Fig. 5.1 Abrasion crater of a sputtered thin film (25Al/75Cr at -40V bias)

As mentioned in section 4.1.4, the first magnetron sputtered depositions were used to find the most favourable setting. This includes the variation of nitrogen partial pressure in the range of 0% (100% Ar) up to 100% N_2 (1Pa).

During these depositions the 70/30 target, a bias voltage of -100V was applied and the sputter power was adjusted to 4 kW (26 Wcm^{-2}).
The deposition with 100% Ar (non-reactive deposition) results in the highest mass loss of the target (0.120 g/min), whereas with increasing nitrogen partial pressure the erosion rate was reduced to 0.020 gram per minute (100% N_2). This decrease in mass loss at higher amount of N_2 can be predominantly attributed to the target poisoning effect, where an increased coverage of the target with nitrides results in a lower sputtering yield. Also the different mass (impulse) of the impinging ions (Ar>N) might result in minor differences. As consequence the nitrogen fraction for the further magnetron sputtered depositions was fixed at 25%. In the following, all synthesized coatings were deposited using the adjustments summarized in Tables 4.1 and 4.3.
The deposition rate means the gain in coating thickness per time, depending on target composition, discharge voltage and bias voltage applied [61]. The parameters influencing the deposition rate as well as mass loss of the targets and gas consumption are summarized in Tables 5.1 and 5.2 for both magnetron sputtering and cathodic arc evaporation, respectively. As mentioned earlier, the total pressure used in magnetron sputtering was held constant at 1 Pa, consisting of 25% N_2 and filled up with Ar. This is equivalent with a N_2 gas flow of 92 sccm and an Ar flow of 226 sccm.

Table 5.1 Parameters influencing the deposition rate in sputtered thin films

Target [Al/Cr]	mass loss [g/min]	$I_{bias\ at\ -40V/-100V/-150V}$ [A]	N_2 flow [sccm]	Ar flow [sccm]	$U_{discharge}$ [V]
25/75	0.10	0.9/1.0/1.2	92	226	300
70/30	0.05	1.2/1.5/1.6			
85/15	0.03	1.2/1.4/1.7			

The erosion rate decreases for both techniques with increasing Al content in the target due to the lower sputtering yield of aluminium (0.6) compared to chromium (1.4) [62]. But nevertheless the mass loss during arc evaporation is much higher. For magnetron sputtering the mass loss is reduced to the third with increasing Al content, whereas using the arc technique the erosion rate is just reduced to the half, which is initially surprising due to the much lower melting point of Al. Generally it can be said that the erosion rate is a sensitive balance between Al, Cr, AlN and CrN (poisoning rate). The bias current (I_{bias}), which is a qualitative indicator for the ion current density at the substrate, increases slightly with rising bias voltage [40]. The nitrogen pressure of 3.5 Pa during arc evaporation was maintained by an N_2 flow of 1050 sccm.

As mentioned earlier during magnetron sputtering a power of 4 kW is used, whereas with arc evaporation the applied power is approximately 2.8 kW. Consequently, comparing the erosion rate and the applied power of both deposition techniques, the arc evaporation technique is more efficient.

Table 5. 2 Parameters influencing the deposition rate in arced coatings

Target [Al/Cr]	mass loss [g/min]	$I_{bias\ at\ -40V/-100V/-150V}$ [A]	N_2 flow [sccm]	$U_{dis.\ at\ 140A}$ [V]
25/75	0.17	3.7/4.0/4.2	1050	20.4
70/30	0.13	3.2/3.6/3.8		
85/15	0.08	3.0/3.4		

In Tables 5.3 and 5.4 the thickness and deposition rates of coatings synthesized by magnetron sputtering and arc evaporation are listed. It can be seen that the deposition rate of the arc evaporated films is about five times higher than for the sputtered ones. For both, magnetron sputtering and arc evaporation, it can be seen that with increasing negative bias voltage and with rising Al content of the target, the growth rate decreases. The decrease of the deposition rate with increasing bias voltage is a well known effect, and correlates with an increase of resputtering of the deposited film due to an increase of the dissipated bias power on the surface of the substrate [63]. It is also shown that the bias current is increased (Table 5.1 and 5.2), due to the complex geometry of the substrate carrousel and the increased sheath effect.

Table 5.3 Thickness and growth rate of sputtered Al-Cr-N coatings

Deposition number	Target [Al/Cr]	Bias voltage [V]	Coating time [min]	Coating thickness [µm] (± 0.1µm)	Growth rate [nm/min]
D222	25/75	-40	40	2.6	65
D206	25/75	-40	200	13.1	65
D223	25/75	-100	40	2.3	60
D205	25/75	-100	200	12.0	60
D224	25/75	-150	40	2.0	50
D207	25/75	-150	200	10.0	50
D216	70/30	-40	40	1.2	30
D183	70/30	-40	60	2.0	30
D196	70/30	-40	200	6.3	30
D217	70/30	-100	40	1.1	25
D195	70/30	-100	200	5.5	25
D221	70/30	-150	40	0.8	20
D197	70/30	-150	200	5.1	20
D214	85/15	-40	40	1.1	25
D199	85/15	-40	200	5.0	25
D215	85/15	-100	40	1.1	25
D237	85/15	-100	60	1.1	25
D234	85/15	-100	110	2.6	25
D208	85/15	-150	40	1.0	20
D233	85/15	-150	60	1.1	20
D225	85/15	-150	110	2.2	20
D203	85/15	-150	200	4.1	20

Table 5.4 Thickness and growth rate of arced Al-Cr-N coatings. The deposition, using the arc evaporation technique with the 85/15-target and -150V bias failed.

Deposition number	Target [Al/Cr]	Bias voltage [V]	Coating time [min]	Coating thickness [µm] (± 0.1µm)	Growth rate [nm/min]
D242	25/75	-40	30	8.5	280
D243	25/75	-100	30	8.0	260
D246	25/75	-150	15	3.5	230
D265	70/30	-40	15	3.0	215
D239	70/30	-40	40	9.0	215
D270	70/30	-100	5	1.0	210
D266	70/30	-100	15	3.3	210
D240	70/30	-100	30	6.1	210
D245	70/30	-150	15	3.0	200
D267	85/15	-40	15	3.0	205
D241	85/15	-40	30	6.5	205
D278	85/15	-100	5	0.9	200
D244	85/15	-100	30	6.0	200

5.2 Coating morphology

5.2.1 Magnetron sputtered coatings

To get information about the surface structure and possible growth defects, SEM investigations were carried out. In the Fig. 5.2a-c SEM micrographs of the surface and fracture cross section of a magnetron sputtered coating shown. For all measurements accomplished on magnetron sputtered coatings low roughness and only few particles were found. It can be seen from Fig. 5.2a that sputtered films are almost free from defects. Looking at the micrographs obtained from the fractured surface (Fig. 5.2b and c) the columnar structure is evident. With all target compositions the structure consists of densely packed columnar grains.

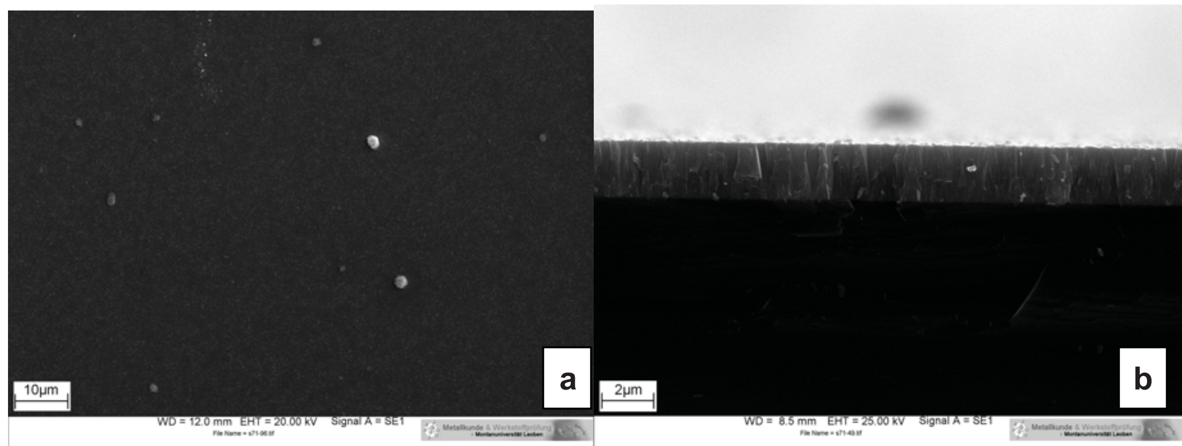

Fig. 5.2 SEM micrograph of sputtered coating synthesized with the 70Al/30Cr target composition and a bias voltage of -40V. **a)** surface, **b)** fracture cross section

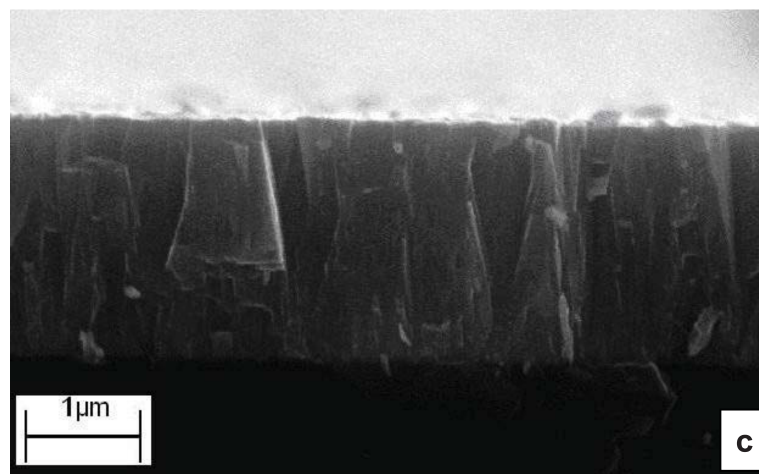

Fig. 5.2 c enlarged view of fracture cross section

5.2.2 Arc evaporated coatings

A main disadvantage of arc evaporated coatings are the molten globules (droplets) ejected from the cathode, which upon incorporation result in growth defects extending through the remainder of the film. Figures 5.3a-c show the surface condition and the fracture cross section of arc evaporated coatings.

In Fig. 5.3a the surface of the coating, synthesized by arc evaporation using the 70Al/30Cr target, is shown. With this target composition, defect sizes up to 4µm and rather high droplet densities can be found. Looking at the fractured surface of the coating synthesized with the 70Al/30Cr target and -40V bias (Fig.5.3b and c) a more dense structure as in sputtered coatings can be observed.

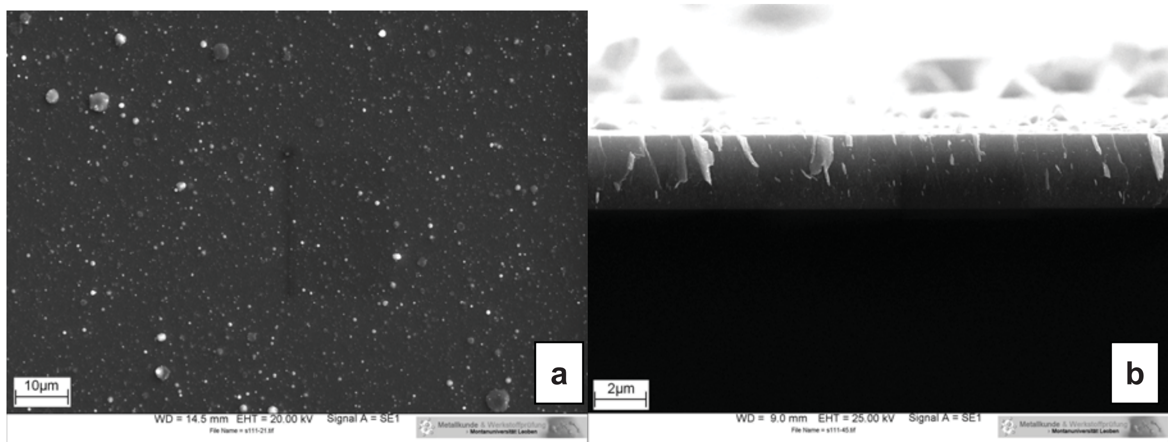

Fig. 5.3 SEM micrograph of an arc evaporated coating synthesized with the 70Al/30Cr target composition and a bias voltage of -40V. **a)** surface, **b)** fracture cross section

Fig. 5.3c) enlarged view of fracture cross section

Basically, increasing Al content leads to a decrease of the droplet size on the coating with an upper limit of about 4 microns and the surface roughness is also reduced. Low aluminium fraction in the target (25at% Al) results in higher droplet size (up to 7 microns) and density, most probably caused by higher porosity in the 25Al/75Cr target.

Münz et al. found that the size and the density of the macroparticles depend on the melting point of the particular droplet material [27]. For Al with a melting point of 660°C they observed a maximum droplet size of about 10 to 20µm and almost $25 x 10^3 mm^{-2}$ droplets and for the higher melting chromium (1870°C) the upper limit of the particle size is one micron and the droplets per area is about $10 x 10^3 mm^{-2}$. The differences to our observations can be explained by the high quality of powder-metallurgical prepared Al-Cr targets used.

In general surface roughness influences the performance of thin films. SEM micrographs revealed smooth surfaces for the magnetron sputtered Al-Cr-N coatings, whereas for the arc evaporated coatings rough surfaces were found. This roughness results from the macroparticles produced during the arc evaporation process. Therefore roughness measurements were carried out on the arc evaporated films. The surface roughness of the arc evaporated coatings was measured using a white light interferometer as described in the experimental part of this work (section 4.2.3). In Fig. 5.4 a three-dimensional plot of an arc evaporated coating surface is displayed.

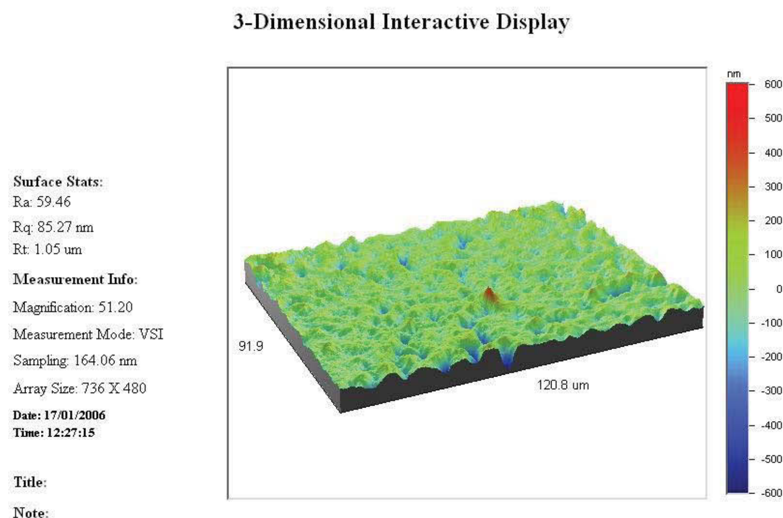

Fig. 5.4 3D-plot of an arced coating surface (70Al/30Cr at -150V bias voltage)

Figure 5.5 presents the arithmetic average value of the surface roughness (R_a) scaled to the respective thickness of the arc evaporated films on Si substrates. The roughness of sputtered coatings was below the detection limits.
Basically it can be said that with increasing deposition time and therefore with increasing coating thickness the surface roughness accumulates.
With increasing bias voltage the thickness equivalent roughness shows upward trend. These results are not in accordance with Hurkmans et al., who showed a smoothening effect on the surface caused by renucleation of film crystals on growth defects by the increased ion bombardment [63]. Thus, it is conducted that the higher values for the 25Al/75Cr target are a sign for higher porosity in the target. Obviously, the material dependent droplet emission is offset by the morphology of the targets.

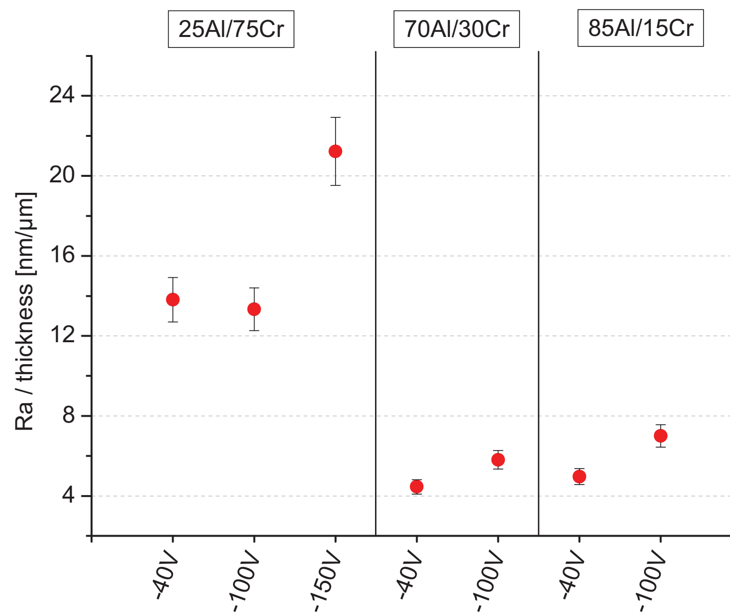

Fig. 5.5 Thickness equivalent roughness of arced thin films

5.3 Coating structure

XRD measurements were performed to determine the crystal structure of the coatings. All coatings investigated by XRD are deposited on high speed steel substrates. In the Fig. 5.6, 5.7 and 5.8 the XRD patterns of Al-Cr-N synthesized by magnetron sputtering and cathodic arc evaporation are presented. To get more detailed information about texture evolution in the Al-Cr-N coatings, texture coefficient calculations were performed (details see section 4.2.4). In Table 5.5 the preferred orientations along with the respective texture coefficients are shown for each sputtered and arc evaporated Al-Cr-N film.

XRD analysis of the Al-Cr-N samples showed that two major crystal structures namely CrN-based (B1 NaCl cubic structure) and AlN-based (hexagonal close packed structure) are detected in the coatings. In Fig. 5.6, the XRD patterns for Al-Cr-N deposited from a target consisting of 25at% Al and 75at% Cr are shown. First of all it must be said that most of these films have high thickness, which can affect the residual stresses within a coating, resulting in a peak movement to lower angles [64]. For this target composition and all bias variations only the cubic $Al_{1-x}Cr_xN$ exists. In general, the smaller Al atom compared to Cr, is embedded at the face-centered site in the cubic CrN and results in a contraction of the lattice. Applying low bias voltage to the substrate (-40V) results in a (200) preferred orientation in the magnetron sputtered coating (Fig. 5.6a). However in the arc evaporated coating (Fig. 5.6b), the (111) orientation additionally occurs with the (200) texture (Table 5.5). With increasing bias voltage the texture coefficient of the (200) orientation decreases and at -150V bias the (111) texture dominates in both, the sputtered and arc evaporated coating.

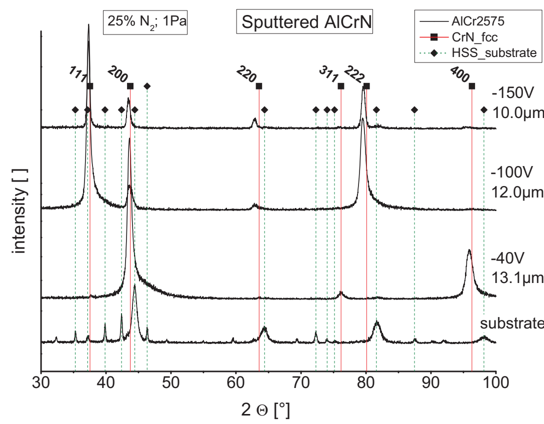

(a) Magnetron sputtered AlCrN coatings

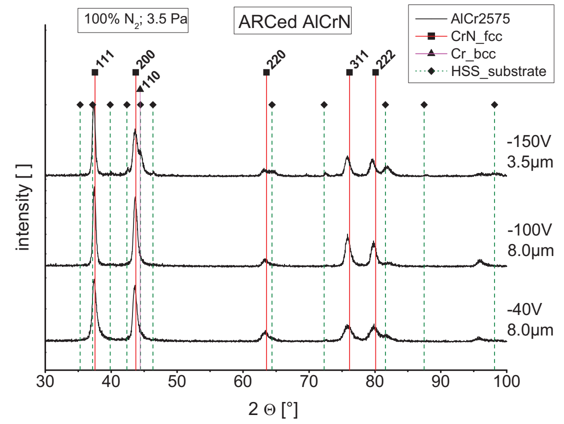

(b) Arc evaporated AlCrN coatings

Fig. 5.6 XRD patterns of AlCrN thin films synthesized using the 25Al/75Cr target

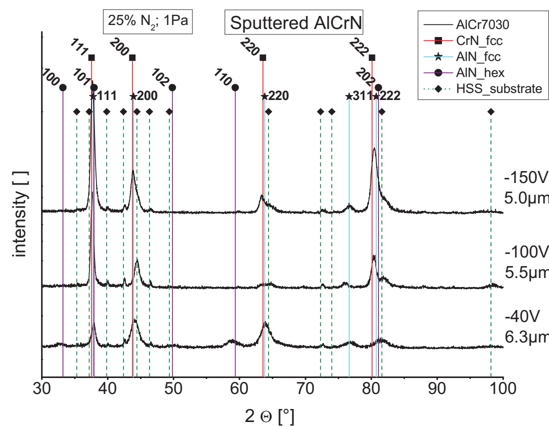

(a) Magnetron sputtered AlCrN coatings

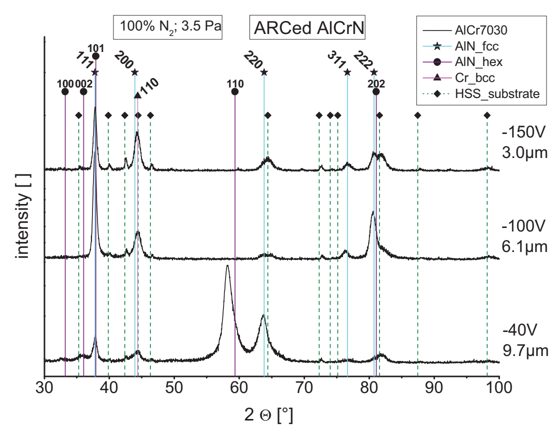

(b) Arc evaporated AlCrN coatings

Fig. 5.7 XRD patterns of AlCrN thin films synthesized using the 70Al/30Cr target

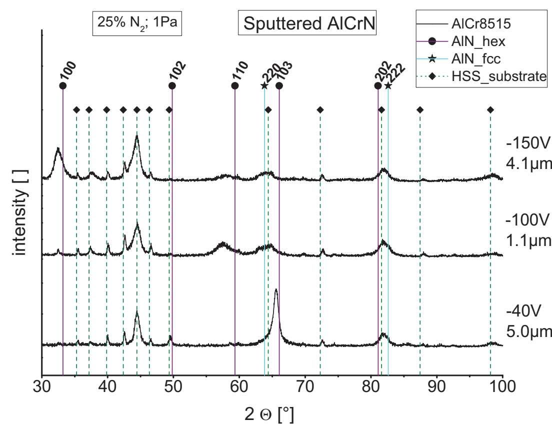

(a) Magnetron sputtered AlCrN coatings

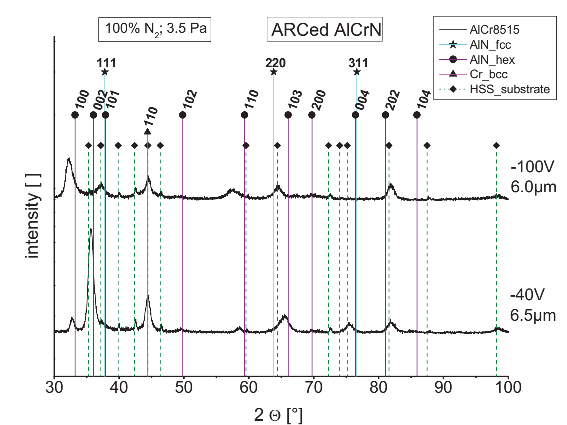

(b) Arc evaporated AlCrN coatings

Fig. 5.8 XRD patterns of AlCrN thin films synthesized using the 85Al/15Cr target

It seems that with increasing bias voltage the growth of the (111) orientation is promoted, caused by the higher energy of the ion bombardment [65] which favours the most densely populated planes. Additionally, a small shift of the measured diffraction peaks toward lower 2Θ-angles was observed with increasing bias voltage. This is a sign for the development of compressive stresses [64].

Table 5.5 Preferred orientation and texture coefficient of synthesized Al-Cr-N coatings

target [Al/Cr]	bias voltage [V]	preferred orientation		texture coefficient	
		sputtered	arc evaporated	sputtered	arc evaporated
25/75	-40	(200), cubic	(200), cubic (111), cubic	2.31	1.77 1.58
	-100	(111), cubic (200), cubic	(111), cubic (200), cubic	1.62 1.64	1.53 1.79
	-150	(111), cubic	(111), cubic	1.54	1.62
70/30	-40	(110), hex (111), cubic	(110), hex (111), cubic	1.29 1.45	0.99 1.61
	-100	(111), cubic (200), cubic	(111), cubic	1.68 1.00	1.74
	-150	(111), cubic	(111), cubic	1.77	1.73
85/15	-40	(103), hex	(100), hex (110), hex	1.00	1.88 1.03
	-100	(100), hex (110), hex (220), cubic	(100), hex (110), hex	1.00 0.63 1.00	1.63 0.74
	-150	(100), hex (110), hex (220), cubic		1.00 0.24 1.00	

Increasing the Al content of the target to 70at%, the XRD patterns in Fig. 5.7 were obtained from coatings with a thickness of 3 to 9 µm. Applying a bias voltage of -40V to the substrate results in a mixture of metastable cubic Al-Cr-N and hexagonal (hex) $Al_{1-x}Cr_xN$. The phase fraction of cubic and hexagonal Al-Cr-N is displayed in Fig. 5.9, for both magnetron sputtered and arc evaporated coatings, obtained from Rietveld refinement. It can be seen that in the arc evaporated film the hexagonal content is predominant for that target composition. Obviously a partial transition from cubic phase to hexagonal phase has occurred. This phase transition takes place if the solubility limit of AlN in the cubic CrN phase is exceeded [66], which is theoretically predicted to be 77% [67].
The metastable cubic $Al_{1-x}Cr_xN$ is predominated by the close packed (111) orientation and the hexagonal $Al_{1-x}Cr_xN$ prefers the (110) texture (Table 5.5).

Due to the small width of the cubic (111) peak it can be assumed that the grain size is relatively high. The hexagonal (110) peak is broader than the cubic (111) peak and therefore the grain size seems to be smaller. At a bias voltage of -100V results the hexagonal phase has disappeared. Looking at the XRD pattern of the magnetron sputtered coating with an applied bias voltage of -100V, two cubic AlN orientations are favoured and these are the (111) and the (200) texture, obtained from texture coefficient calculations. But due to the higher texture coefficient of 1.68, the (111) orientation is preferred. For the corresponding arc evaporated coating only one phase, the cubic AlN exists. The predominating texture for these adjustments is (111), which is confirmed by an increasing texture coefficient. With the highest bias voltage applied (-150V) the same phase and the equal orientation as for -100V were observed. Basically it can be assumed that with increasing bias voltage the cubic phase is favoured, resulting in a more dense structure. The bias increase is also connected with defect generation and might contribute to a higher solubility limit of the metastable fcc Al-Cr-N and as a result the hex Al-Cr-N phase fraction becomes diminished [68].

The preferred textures, obtained with the 25Al/75Cr and 70Al/30Cr target do not correlate with the results shown by Hurkmans et al. and Gautier et al. [63, 69]. They revealed a texture change for cubic CrN from (111) to (220) with increasing bias voltage.

For a target composition consisting of 85at% Al and 15at% Cr the XRD pattern in Fig. 5.8 were recorded. The coating thickness ranges from 1.1 up to 6.5 microns. Applying a negative bias voltage of -40V during magnetron sputtering leads to the hexagonal $Al_{1-x}Cr_xN$ phase with the (103) texture as preferred orientation (Fig. 5.8a). In contrast, with the arc evaporation technique two orientations of the hex $Al_{1-x}Cr_xN$ phase exists (Fig. 5.8b). These are the (100) and (110) texture. But from the texture coefficient calculations it was evident, that the (100) orientation is preferred (Table 5.5). With these adjustments the phase fraction completely consists of hex $Al_{1-x}Cr_xN$, as proposed in [66, 67].

Increasing the bias up to -100V revealed no change in texture and phase fraction of the arc evaporated coating. But with magnetron sputtering the orientation of the hex AlN changed to the favoured (100) texture and additionally to the hexagonal phase a cubic $Al_{1-x}Cr_xN$ phase could be observed. The adjusted orientation of this cubic CrN is (220). A further increase of bias to -150V leads to no transformations.

In all arc evaporated films the small peak at $2\Theta = 44.5°$ could be an indication of pure chromium (Cr), showing the existence of unnitrited macroparticles [70].

5.3.1 Phase fraction, lattice parameter

To get information about the phase composition in the coating Rietveld refinement was carried out. The results are shown in Fig. 5.9. Using the target composition with 70at% Al and a bias setting of -40V a phase mixture for both arc evaporation and magnetron sputtering is present. But with arc evaporation the hexagonal part is about 72 wt% and compared to the sputtered coating with 4 wt% much higher. The remaining coatings with the 70/30 target are built up as cubic structure. With a higher Al content in the target (85at%) the hexagonal structure dominates. Nevertheless with magnetron sputtering and a bias voltage of -100V cubic phase fractions were found.

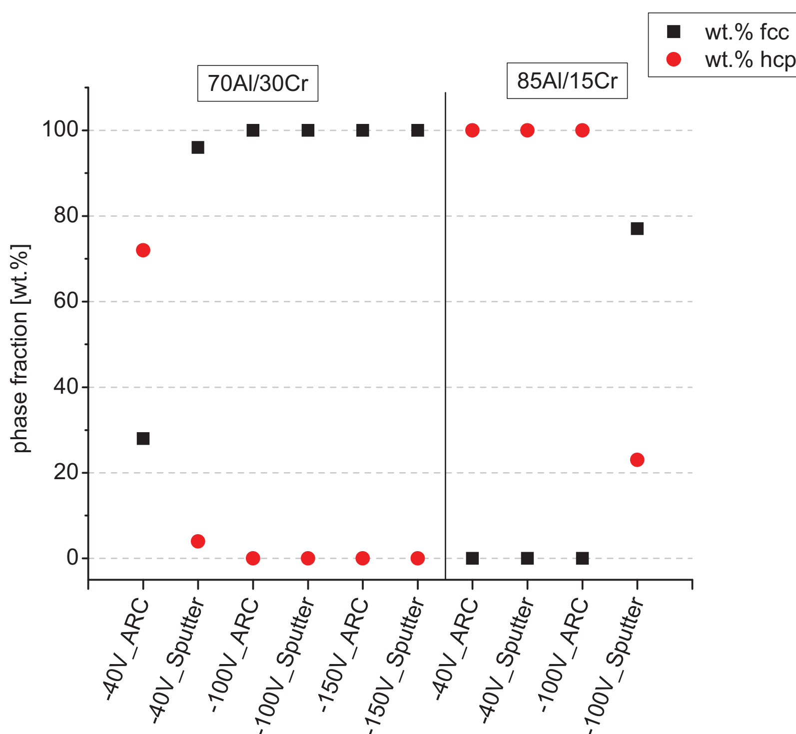

Fig. 5.9 Rietveld phase composition of Al-Cr-N coatings

Additionally to phase fraction, the lattice constants can be determined with the Rietveld method. It was found that the lattice constants decrease with increasing Al in the cubic structure of Al-Cr-N from approximately 4.15Å to 4.11Å. But within the hexagonal structure of Al-Cr-N the lattice constants of the nitride increases with increasing Al content. In the a-direction the lattice expands from 3.12Å to 3.18Å and in c-direction the value increases from 4.95Å to 5.12Å within the hexagonal structure.

These lattice-constant-changes in the Al-Cr-N films are due to the ion radius difference between Al and Cr ions [71].

Furthermore the Rietveld measurements have shown that with increasing bias voltage the cubic lattice constant increases for Al-Cr-N synthesized by magnetron sputtering, which may caused by interstitial argon particles [72]. On the contrary, in the arc evaporated Al-Cr-N films a decrease of the cubic lattice constant with increasing bias voltage was observed, probably due to high stresses. With both deposition techniques the hexagonal lattice constants increases with a higher bias applied, caused by an increased defect generation.

The crystallite size of the films ranged from 11 to 110 nm, whereby smaller grain sizes are observed for higher aluminium content.

5.4 BSTM measurements

5.4.1 Residual stresses

For the determination of residual and intrinsic stress in the coating, biaxial stress temperature measurements (BSTM) were carried out. Additionally the linear thermal expansion coefficient α was calculated from the stress built up in the coating due to the different thermal expansion of substrate and coating.

The investigated coatings were synthesized using the settings summarized in Tables 4.1 and 4.3 for magnetron sputtering and arc evaporation, respectively. As substrate served a small silicon plate (Si), on which the Al-Cr-N film was deposited.

In Fig. 5.10 an example of a heating and cooling sequence of a recorded beam bending measurement is shown. Before heating, at room temperature (~28°C) the residual stress $\sigma_{residual}$ in the coating is shown. At higher temperatures the diffusity is increased and at a certain temperature the recovery process is started resulting in stress relaxation and defect annihilation. This onset of recovery is shown in the graph at about 500°C where the curvature changes. Recovery leads to a reduction of compressive stresses caused for example by Frenkel pairs and other point defects. At 500°C, that means at deposition temperature, the value of the intrinsic stress $\sigma_{intrinsic}$ is shown. After heating up to 700°C the cooling sequence begins, in which linear elastic behaviour occurs. Thus the linear thermal expansion coefficient $\alpha_{(cooling)}$ can be found out from the cooling sequence. During further cooling the formation of tensile cracks can be observed, seen by the gradual decrease of stress.

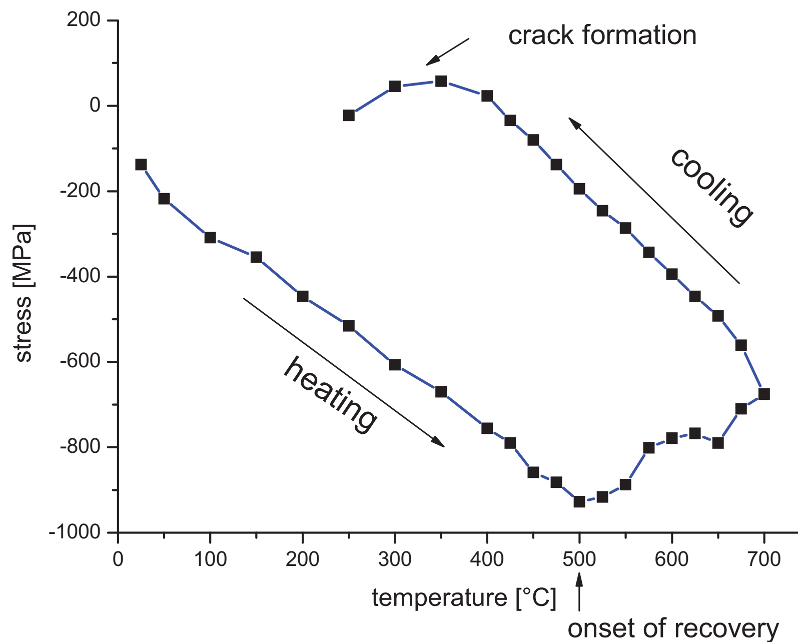

Fig. 5.10 Stress vs. temperature of arced Al-Cr-N synthesized using the 25Al/75Cr target and a bias of -40V, deposited on Si (100) substrate

As mentioned in the experimental part (section 4.2.5), effects contributing to the residual stresses are thermoelastically-induced stresses due to different coefficients of thermal expansion between coating and substrate, mechanically-induced stresses (phase transformation or precipitation during cooling) and growth-induced stresses [64]. Within this measurement the main stress fraction can be attributed to growth defects and thermoelastic contributions [64]. In Fig. 5.11 the residual stresses at room temperature of sputtered and arc evaporated Al-Cr-N deposited on silicon plates are schematically shown. The thickness of the investigated films varied from 1µm up to 3µm. All stress values obtained are negative, with the exception of the coating sputtered from the 25Al/75Cr target and a bias voltage of -40V. As can be seen from Fig. 5.11 the compressive stresses increase with increasing bias voltage, due to the higher energy of the impinging ions and the subsequent defect generation. This higher ion energy results in direct and knock-on subplantation of nitrogen and argon ions in case of magnetron sputtering and metal and nitrogen ions in the arc evaporation process, respectively [73]. As a consequence the density and the compressive stress of the film increase [63]. Further increase of bias (-150V) results in a decrease of residual stress as shown for the sputtered coatings. The process responsible for this drop off could be relaxation and resputtering caused by the increased ion bombardment [73].

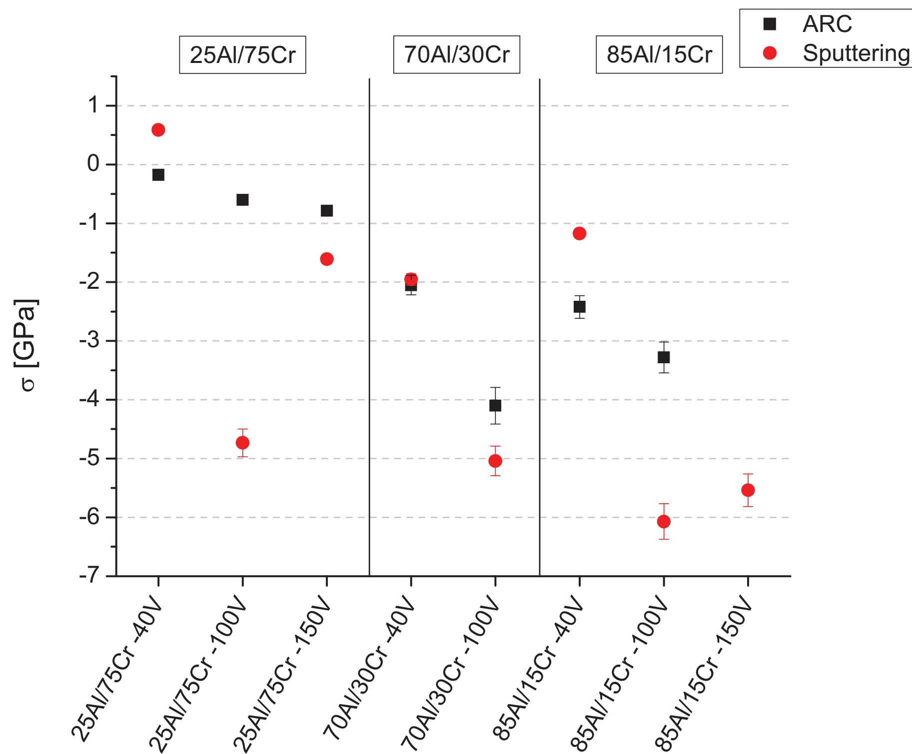

Fig. 5.11 Residual stresses in Al-Cr-N coatings deposited on Si (100) substrate

Looking at the Al fraction of the targets it can be seen that within the cubic structure (Al content up to 70at%), the compressive stresses increase due to defect generation (arcing) and/or argon incorporation (sputtering) in the lattice. For higher amount of Al (85at%), the solubility limit of Al in CrN is exceeded and therefore transformation to the hexagonal structure occurs [66]. The stress values obtained with this target composition are similar to the achieved values using the 70Al/30Cr target, resulting in residual stresses of almost -6 GPa. Summarized it can be said that the compressive stresses increase with bias and the stresses in sputtered coatings are higher compared to arc evaporated films. A reason therefore is that during arc evaporation the bombardment of the growing film with highly energized aluminium and chromium particles causes not only a dense structure but also supports the recrystallization of buried amorphous material, resulting in a decrease of the compressive stresses [35]. The high stresses in sputtered films are caused by accelerated argon ions incorporated on interstitial sites and by point defects.

5.4.2 Linear thermal expansion coefficient

The linear thermal expansion coefficient (α), calculated from the approximately linear stress range in the cooling sequence of the beam bending curve, is shown in Fig. 5.12.

Considering the linear thermal expansion coefficient (α) calculated for the target composition with the lowest Al content it can be seen that the arc evaporated coatings revealed higher thermal expansion (approximately $1.6x10^{-5}K^{-1}$ for arc evaporation and $1.1x10^{-5}K^{-1}$ for magnetron sputtering). The targets with higher Al fraction reached similar coefficients for both deposition techniques.

With a target composition consisting of 85at% Al and 15at% Cr the coefficient is lower compared to the value achieved with smaller Al content, reaching a thermal expansion coefficient in the order of $8.5x10^{-6}K^{-1}$ for both techniques (green dashed line in Fig. 5.12). A possible argument for this behaviour could be the change from the cubic to the hexagonal structure.

Finally it must be mentioned that numerous source of error exist during the determination of the thermal expansion coefficient. One of these sources is the elastic modulus of the coating (E_C), which was received from the hardness measurements (section 4.2.6). Therefore an average thermal expansion coefficient of $1.41x10^{-5}K^{-1}$ can be assumed for the films deposited from the 25Al/75Cr and 70Al/30Cr target (blue dashed line in Fig. 5.12). The literature values for the linear thermal expansion coefficient of hex AlN and fcc CrN respectively ($1.05 \pm 0.05x10^{-5}K^{-1}$), are in good agreement with the obtained values [74].

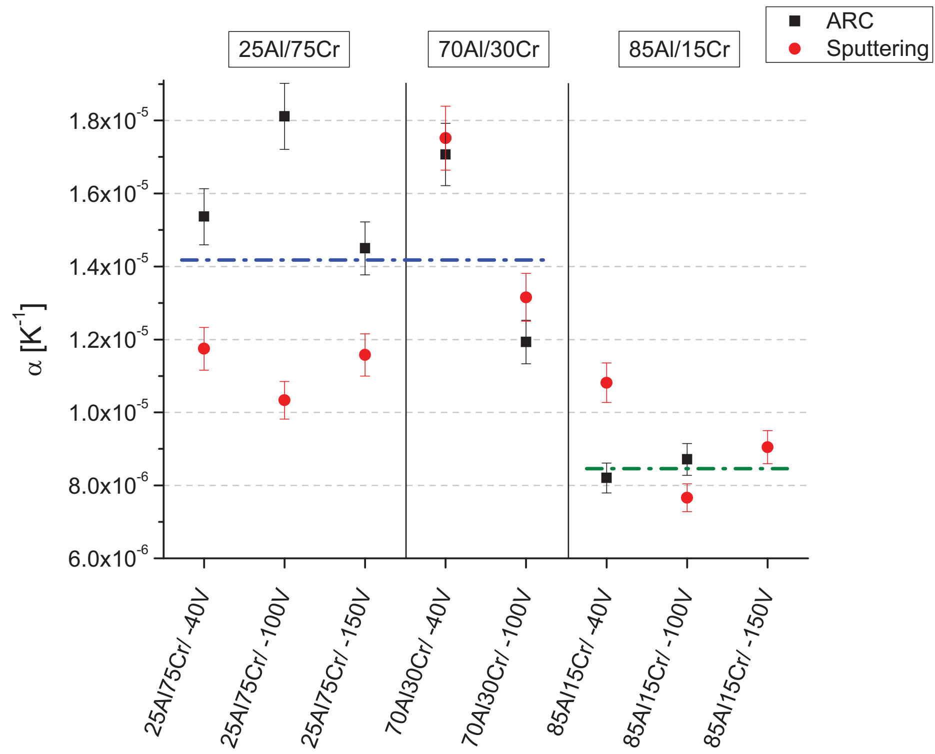

Fig. 5.12 Linear thermal expansion coefficient (α) of Al-Cr-N thin films

5.5 Nanoindentation (hardness and modulus)

5.5.1 Magnetron sputtered coatings

As mentioned in the experimental part of this work the hardness was measured using a Fischerscope H100C on high speed steel substrates. The hardness measurements were realized at constant indentation depth (0.5 microns) to circumvent some of the calibration issues (further details in section 4.2.6). In Fig. 5.13 Hardness (HUpl) and modulus of the sputtered Al-Cr-N coatings are shown. Basically hardness varies with the structure of the thin film. Metastable phases, such as cubic Al-Cr-N, are determined by the incorporation of nitrogen in interstitial lattice sites and the generation of supersaturated solid solutions [35]. The incorporation of interstitials affects the lattice (distortion) and the initiation of dislocation movement resulting in increased hardness. PVD grown films show preferred orientations and these textures have influence on hardness. Another important effect is the strain hardening via the substitution of Cr by smaller Al atoms, while also the generally reduced grain size might contribute (Hall-Petch) [16].
Using the Cr-rich target (75at%) hardness is not much higher than 21 GPa due to the cubic $Al_{1-x}Cr_xN$ structure [75]. With an Al-rich target composition (70at% Al) highest hardness values (~28 GPa) were achieved, due to solid solution hardening, at predominating (crystalline) cubic $Al_{1-x}Cr_xN$ phase. Up to an Al content of 70% the hardness increased monotonously at moderate bias (≤ -100V). Correspondingly the lattice constant decreased due to the incorporation of Al in the cubic lattice. Additionally the decreasing grain size also contributes to the hardness increase [2].
Using the target with the highest aluminium content (85at%), the hardness values are low in comparison to the 70Al/30Cr films. This is due to the change from cubic to the mechanically less favourable hexagonal crystal structure, especially at a low bias voltage. The results obtained are in good agreement with earlier measurements [75].
For all target compositions it can be said that with increasing bias voltage the hardness increases, even if the values of the coatings deposited from the targets with 25 and 70at% Al and a bias of -150V are lower than the hardness achieved with a bias of -100V. In general, the Al-Cr-N coatings synthesized with lower bias voltage (-40V) are softer, due to an underdense structure. The main effect influencing the hardness could be defect hardening. That means, with increasing bias the kinetic energy of the impinging particles (Ar ions) is high enough creating different kinds of lattice defects in the growing layer. For example nitrogen atoms are pushed from regular lattice sites, occupied by the Ar ions, and embedded as interstitials.

As consequence high compressive residual stresses are initiated in the coating (section 5.4). The slight decrease in hardness at -150V bias voltage could be referred to the higher ion bombardment, resulting in re-sputtering and renucleation [73]. In addition stabilization of the defect density for bias higher than -100V might arise.

The Young's modulus was also measured reaching a value of about 330 GPa for a 70Al/30Cr target composition and -100V bias (Fig. 5.13). However, due to calibration issues of the instruments the modulus values should be used for a qualitative comparison only [58].

Finally it must be mentioned that the fluctuations are rather high as can be seen from the error bars drawn for each value.

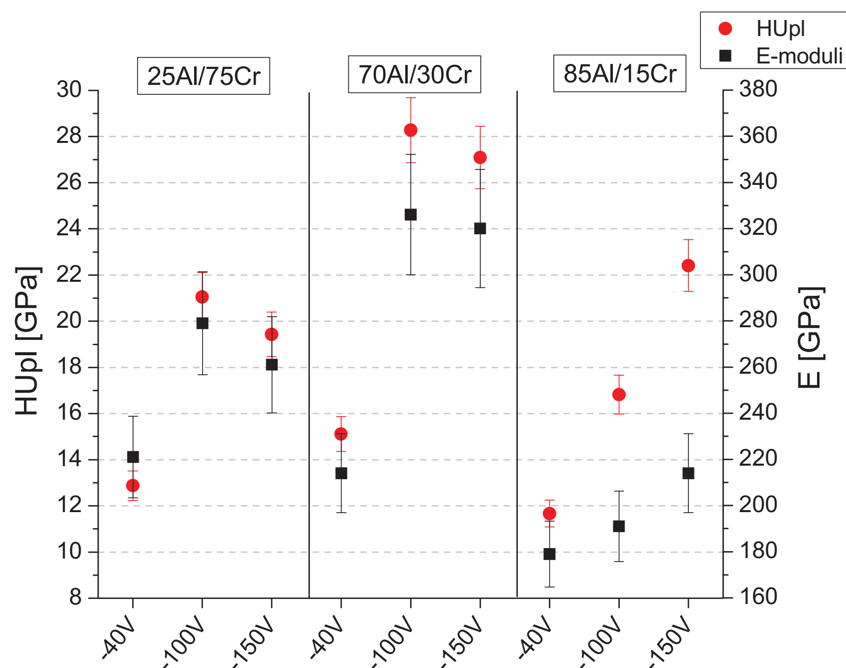

Fig. 5.13 Hardness and young modulus of sputtered Al-Cr-N coatings

5.5.2 Arc evaporated coatings

The hardness and modulus of the arc evaporated coatings was measured using the same adjustments on the Fischerscope as for magnetron sputtered thin films. In Fig. 5.14 the hardness and Young's modulus of arced films are illustrated. Generally the hardness values obtained from arc evaporated coatings are lower in comparison to the sputtered ones, caused among others by macroparticles embedded on the coating surface. Rotating the carrousel during deposition would result in a decrease of the droplet density in arc evaporated thin films but was not used for comparative reasons.

Similar to magnetron sputtering the hardness increases with the bias voltage. With a target composition consisting of 25at% Al and 75at% Cr the lowest hardness values were observed. Increasing the Al-content in the target to 70 at% results in highest hardness achieved (~24 GPa). Applying only a moderate bias voltage of -40V during deposition leads to the lowest hardness value within this target composition.
This can be explained with the growing hexagonal phase fraction and a decrease of the cubic phase. Generally the same hardening mechanisms as in magnetron sputtered coatings (defect hardening) are present. But in contrast to magnetron sputtering metal ions (due to high ionization degree) are accelerated by the applied bias voltage and produce lattice defects in the film.
A target consisting of 85at% Al and 15at% Cr supplied only the hexagonal $Al_{1-x}Cr_xN$ phase and therefore mechanical properties are inferior to the cubic structure. For comparison, hardness values for cubic CrN and hex AlN given by Kawate et al. are 15 GPa and 17 GPa, respectively [75].

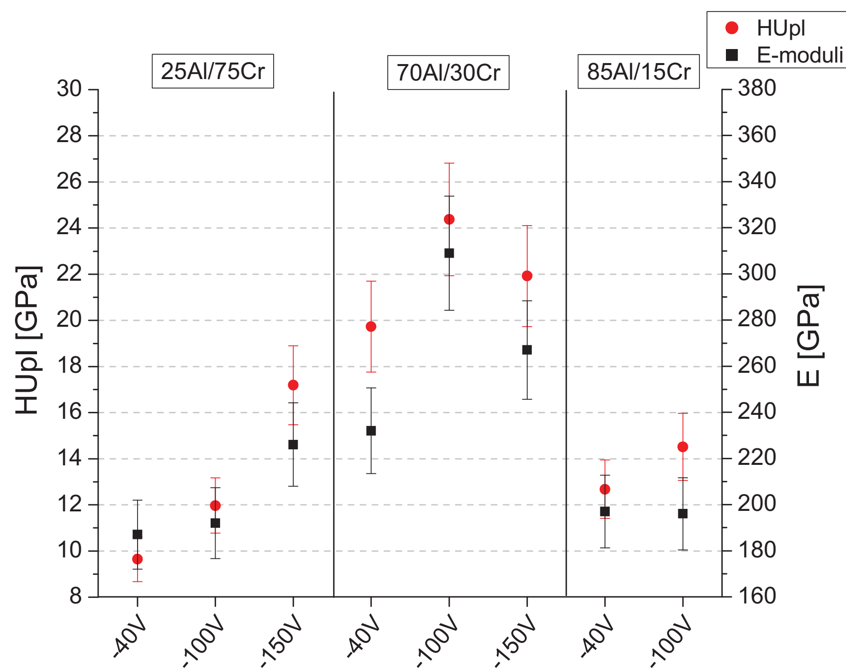

Fig. 5.14 Hardness and Young’s modulus of arc evaporated Al-Cr-N

5.5.3 Comparison of sputtered and arced coatings

Basically it can be said that the limits of variation for arc evaporated coatings is much higher than for sputtered ones. The reason for that could be the large number of macroparticles generated during the arc evaporation process and these particles produce defects which minimize the hardness.

Regarding to the target composition with 25 at% Al, both arced and sputtered films only consist of the cubic $Al_{1-x}Cr_xN$ phase. The hardness values of the sputtered films within this composition are higher then the values obtained from the arced coatings.

Measurements on Al-Cr-N coatings deposited from a target consisting of 70at% Al and 30at% Cr resulted in a higher hardness for the arced coating but restricted to a low bias voltage (-40V). The remaining values for -100V and -150V with the 70Al/30Cr target are higher using magnetron sputtering. Generally the 70Al/30Cr targets provide highest hardness for both arced and sputtered coatings. With the target containing 85at% Al similar values as with the 25Al/75Cr target were reached, even though in targets with 85at% Al the hexagonal structure is predominant.

Summarized it can be said that sputtered Al-Cr-N coatings showed higher hardness than arc evaporated Al-Cr-N coatings and the obtained Young’s moduli are similar. In general the mechanical properties are determined by the phase composition but can be offset by a less favourable morphology. Therefore, the maxima coincide with the highest Al fraction in CrN but are offset, especially at low bias voltage by a presumably voided morphology.

5.6 Plasma investigations

5.6.1 Magnetron sputtered coatings

To get insights about the growth conditions, different measurements were carried out. The process analysis includes the estimation of the incorporation rate $J_{Al\&Cr}$ and the measurement of the ion flux density I_0.

In Fig. 5.15 the incorporation rate of sputtered Al-Cr-N is schematically shown. For the evaluation of the incorporation rate a few assumptions were taken, such as ideal density of the cubic phase (section 4.3.1). The densities used for the determination of the incorporation rate are $5.6\,gcm^{-3}, 4.5\,gcm^{-3}$ and $3.6\,gcm^{-3}$ for the $25at\%\,Al$, $70at\%\,Al$ and $85at\%\,Al$ target. Additionally the growth rate was used to determine the incorporation rate (Table 5.3 and 5.4). From figure 5.15 it can be seen that $J_{Al\&Cr}$ decreases with increasing bias voltage. An increasing Al content in the target results in a reduced number of particles incorporated on the substrate. Therefore, an incorporation rate of about $5.5\,x10^{19}$ atoms per m^2 and second is supplied from the 25Al/75Cr target. This is double as compared to an aluminium content of 70at%. For the target composition consisting of 85at% Al and 15at% Cr, the incorporation rate $J_{Al\&Cr}$ is approximately $1.5\,x10^{19}\,m^{-2}s^{-1}$. As mentioned earlier, the incorporation rate is influenced by the applied bias voltage. The apparent drop in rate at higher bias voltages could be due to resputtering of near-surface bonded Al and Cr atoms [73] but might as well be artificial due to an increased density by, e.g. a denser structure or the hex-fcc transition. The decrease in incorporation with increasing Al content can be explained with the different sputtering yields for aluminium and chromium. The sputter yields for Al and Cr at 500 eV argon ions are 0.6 and 1.4, respectively [62]. As a result the emission rate decreases and consequently the incorporation rate decreases with an increase in Al fraction. This decrease can also be attributed to the target poisoning. The poisoning influences the sputter yields of CrN and AlN due to their formation enthalpy of $-117\,kJmol^{-1}$ and $-318\,kJmol^{-1}$, respectively [74]. The ratio of these enthalpies is in good agreement with the Cr to Al sputter yield ratio.

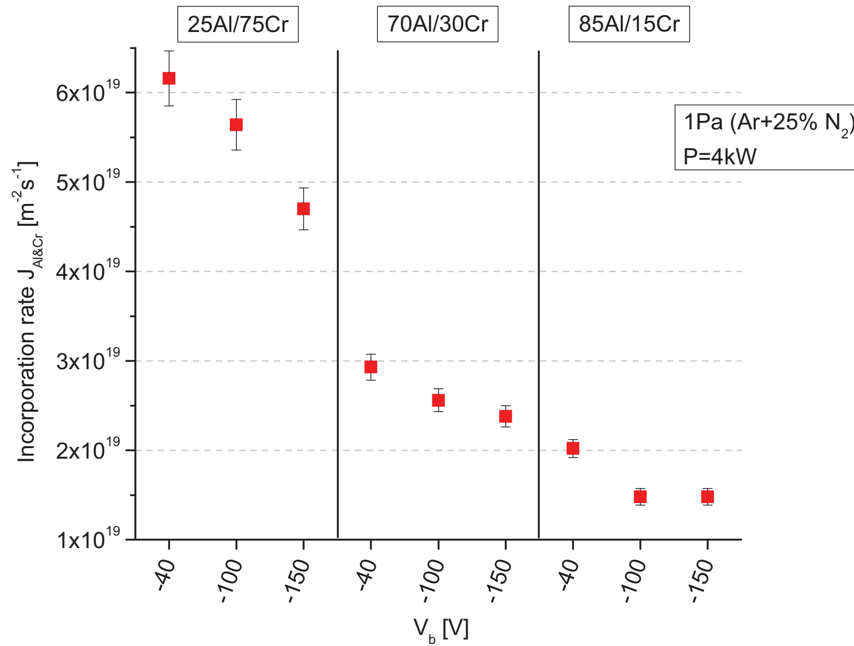

Fig. 5.15 Incorporation rate of sputtered Al-Cr-N coatings

The ion flux density I_0 was measured by a flat probe. The arrangement of the probe mounted in the coating chamber is described earlier in this work (section 4.3).
The used targets for this investigation are the 70Al/30Cr and the 25Al/75Cr target respectively, to consider the influence of the target composition. However, no influence of the target composition could be observed. At the beginning of this measurement the floating potential V_{fl} was determined. With a sputter power of $4\,kW\ (26W \cdot cm^{-2})$, without applied bias voltage to the substrate carrousel, and a pressure of $1Pa\ (25\%\,N_2)$ in the coating chamber of the RCS plant a floating potential of about -15V has been found (all obtained V_{fl} values have negative sign). It should be noted that the values are averaged due to rapid fluctuations (15%). From Table 5.6 it can be seen that within this gas composition and variation of the target power (0.5 up to 4 kW) the floating potential was nearly unaffected.

Table 5.6 Floating potential and electron temperature in 1 Pa (25%N_2) environment

target power [kW]	pressure [Pa]	V_{fl} [V]	+/-	T_e [eV]	+/-
0.5	1 (25%N_2)	-14.6	1.0	3.18	0.03
1.0		-14.7	1.0	3.20	0.03
2.0		-14.8	1.0	3.23	0.03
3.0		-15.0	1.0	3.27	0.03
4.0		-15.4	1.0	3.36	0.03

Table 5.6 also shows the electron temperature T_e calculated from the floating potential. In the coating condition, that means a sputter power of 4 kW and 1Pa (25% N_2), the gas atmosphere T_e is about 3.3 eV. Changing only the atmosphere in the chamber to 100% Ar (1Pa) V_{fl} dropped to -11V and with $1 Pa\ N_2$ the floating potential goes up to approximately -19V (Tables 5.7 and 5.8). The more negative floating potential in pure nitrogen atmosphere (1Pa) could be referred to the smaller diameter of nitrogen resulting in a lower collision probability. Applying a negative bias to the substrate leads to no drastically altering in the floating potential.

Table 5.7 Floating potential and electron temperature in 1 Pa (Ar) environment

target power [kW]	pressure [Pa]	V_{fl} [V]	+/-	T_e [eV]	+/-
0.5	1 (Ar)	-11.1	0.1	2.37	0.03
1.0		-11.2	0.1	2.39	0.03
2.0		-11.8	0.3	2.52	0.05
3.0		-11.6	0.3	2.48	0.05
4.0		-11.7	0.3	2.50	0.05

In pure argon atmosphere (1Pa) the electron temperature is about 2.5 eV (Table 5.7), whereas in nitrogen atmosphere (1Pa) T_e increases with increasing power from 3.3 up to 4.7 eV (Table 5.8).

Table 5. 8 Floating potential and electron temperature in 1 Pa (N_2) environment

target power [kW]	pressure [Pa]	V_{fl} [V]	+/-	T_e [eV]	+/-
0.5	1 (N_2)	-13.9	1.0	3.35	0.05
1.0		-16.5	1.0	3.97	0.05
2.0		-17.2	1.5	4.14	0.1
3.0		-18.3	1.5	4.40	0.1
4.0		-19.5	1.5	4.69	0.1

From Tables 5.6, 5.7 and 5.8 it can be seen that with increasing nitrogen fraction in the deposition chamber the floating potential becomes more negative and as a result the plasma potential reaches a more negative value. In Fig. 5.16 the ion flux density I_0 versus sputter power P characteristics in different atmospheres is shown. The ion flux density was calculated using the current measured on the flat probe.

In pure Ar atmosphere (1Pa) and a target power of 4 kW the influence of bias voltage on the ion flux was investigated. This measurement revealed an increase of the ion flux of about three times by changing the substrate voltage from zero to -40V. Applying a more negative bias showed no significant change in ion flux. Therefore, during the further experiments the substrate voltage was chosen with -80V to ensure being in the ion saturation region.

For all sputtered Al-Cr-N coatings deposited in this work, a sputter power of 4 kW was selected resulting in an ion flux density I_0 of nearly $9.5x10^{19} m^{-2} s^{-1}$ (in 1Pa Ar+ 25%N_2 atmosphere). As can be seen from Fig. 5.16 the ion flux density increases with the sputter power due to an increased number of carriers. But varying the pressure of the sputtering gas or even changing the sputtering gas (N_2) leads to no large variation in I_0 with exception of the measurement in 3.5 Pa nitrogen atmosphere (green pattern). These results are in good agreement with Petrov et al. [76].

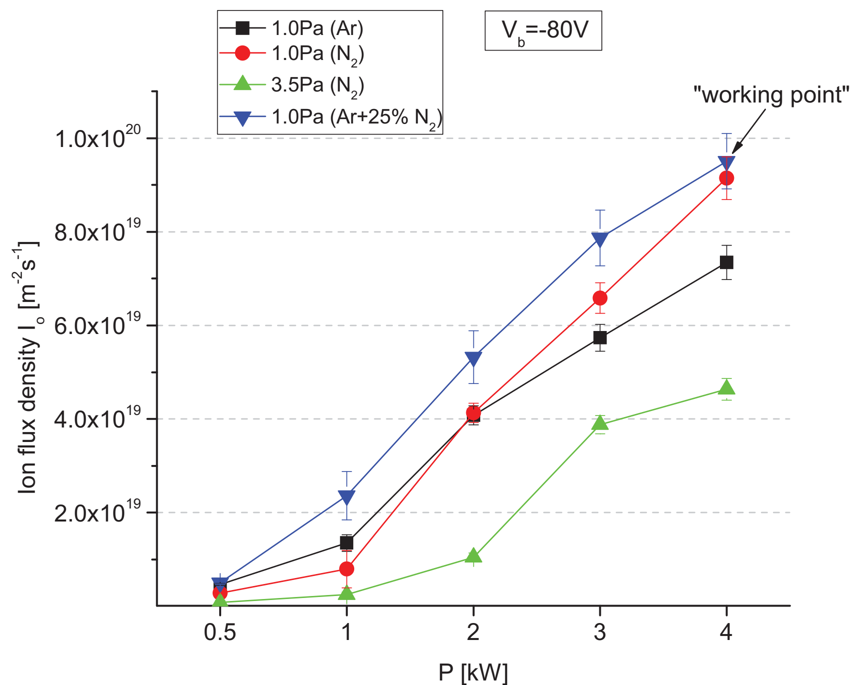

Fig. 5.16 Ion flux density I_0 of sputtered Al-Cr-N coatings

From these measurements the ion assistance α can be calculated. This is the ratio between the ion flux and the neutral atoms impinging on the substrate surface (incorporation rate). For sputtered Al-Cr-N coatings the ion assistance ranges from about 1.5 up to 6.4 (Fig. 5.17). From these measurements it can be derived that with increasing ion energy the ion/atom flux ratio (α) increases. This is due to the high energetic ions (inert Ar ions), impinging on the growing film, causing higher adatom mobility and resputtering of condensing atoms. Another fact is that with a higher amount of aluminium in the target the film growth rate decreases and therefore the ion assistance increases.

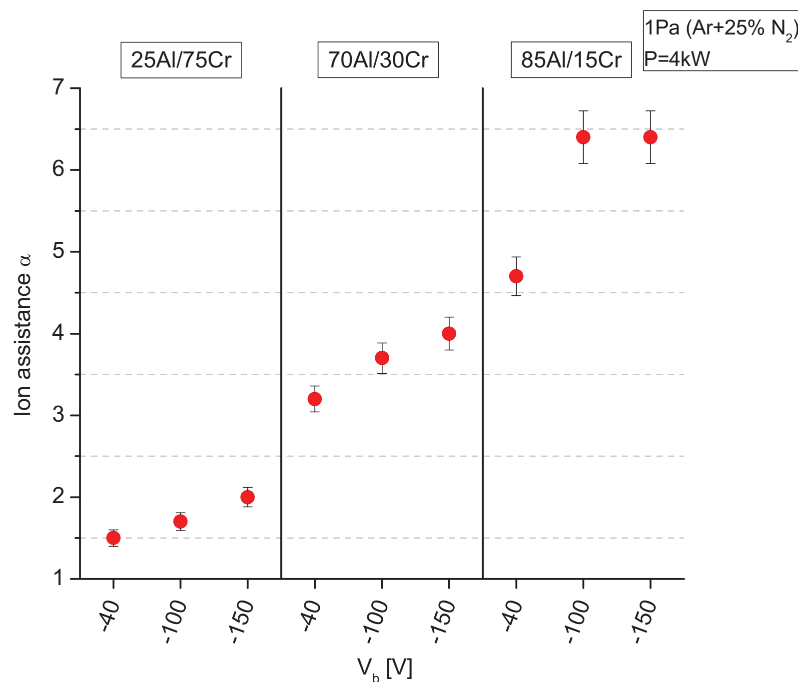

Fig. 5.17 Ion assistance of sputtered Al-Cr-N coatings

Additionally an averaged value of the plasma density (n_i) was calculated by using eq. (6) (section 2.2.1). For magnetron sputtered Al-Cr-N coatings the plasma density (number of ions) is approximately $7.6x10^{16}\,m^{-3}$, which is in good agreement with Olaya et al. [77].

5.6.2 Arc evaporated coatings

To enable a comparison between magnetron sputtering and arc evaporation, the same investigations were carried out using the arc evaporation technique. These tests were realized using the same targets as for magnetron sputtering. In Fig. 5.18, the incorporation rate for arced Al-Cr-N coatings is illustrated. Generally the incorporation rate decreases with decreasing chromium content in the target. From this figure it is also evident that a higher substrate voltage results in a slight decrease of $J_{Al\&Cr}$ maybe caused by incident ions with energy higher than the sputtering yield [78] and/or densification. For the target with the lowest aluminium content, the highest rates are achieved. Within this measurement the incorporation rate ranges from $1.6x10^{20}$ to $2.5x10^{20}$ neutral atoms per m^2 and second. This change in incorporation can be attributed to the target morphology and as consequence to the melting point of the target material.

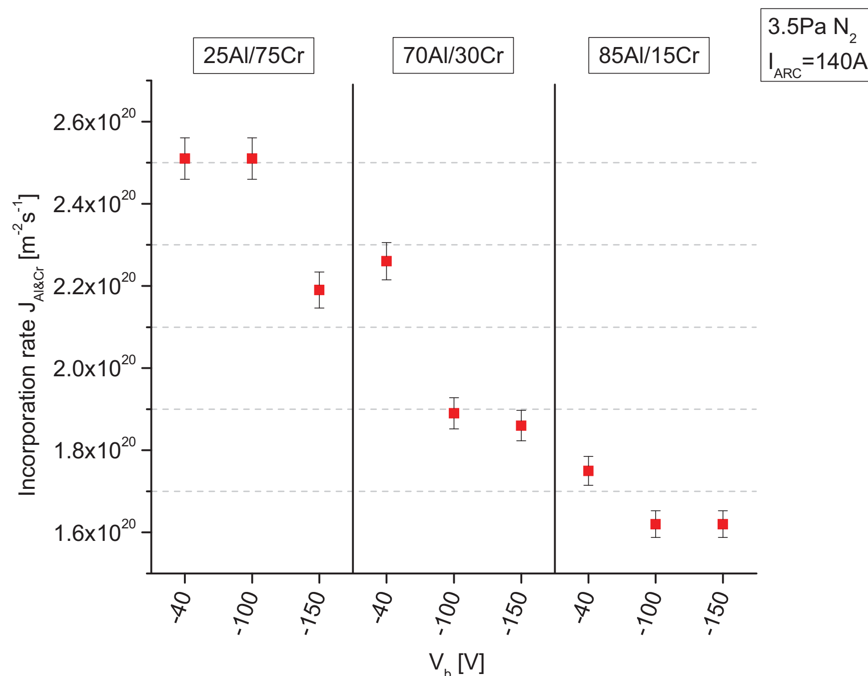

Fig. 5.18 Incorporation rate of arced Al-Cr-N coatings

The planar probe measurement starts with determining the floating potential V_{fl}. Different parameters such as gas, pressure and arc current were varied to show the effect on V_{fl}. During floating potential measurements no bias was applied to the substrate. In Table 5.9 the floating potential is shown for different values of arc current in argon and nitrogen environment, respectively.

By using the arc evaporation method with an inert gas in the coating chamber (1Pa Ar) and increasing arc current (up to 200A), the floating potential also increases. The same effect was obtained with 1Pa nitrogen in the chamber. Basically in arc evaporation mode the floating potential is less negative due to the faster ions. Table 5.9 also shows an increase of the electron temperature with increasing arc current from 2.6 up to 3.4 eV (calculated for nitrogen atmosphere). This increase in electron temperature T_e is coupled with an increased electron motion and results in a larger number of electron-electron collisions and other interactions.

Table 5.9 Floating potential and T_e as a function of arc current (constant pressure)

I_{ARC} [A]	pressure [Pa]	V_{fl} [V]	+/-	pressure [Pa]	V_{fl} [V]	+/-	T_e [eV]	+/-
100	1 (Ar)	-7.35	0.05	1 (N_2)	-11.5	0.3	2.60	0.05
120		-7.80	0.05		-12.5	0.3	2.82	0.05
140		-8.10	0.05		-13.0	0.3	2.93	0.05
160		-8.40	0.05		-13.5	0.3	3.05	0.05
180		-8.70	0.05		-14.4	0.3	3.25	0.05
200		-9.05	0.05		-15.0	0.3	3.39	0.05

With constant arc current (140A) and increasing Ar pressure (up to 2.5 Pa) a decrease of V_{fl} can be observed and as consequence the plasma potential becomes more positive. Using nitrogen gas (0.5 to 3.5 Pa) instead of argon at even 140A leads to a growing floating potential (-17V). The results obtained from these measurements are listed in Table 5.10. In pure nitrogen environment T_e increases with increasing N_2 pressure. Using the deposition condition for arc evaporation results in an electron temperature of 3.86 eV.

Table 5.10 Floating potential and electron temperature as a function of gas pressure

I_{ARC} [A]	pressure [Pa]	V_{fl} [V]	+/-	T_e [eV]	+/-	pressure [Pa]	V_{fl} [V]	+/-
140	0.5 (N_2)	-15.1	0.3	3.41	0.05	0.5 (Ar)	-9.70	0.05
	1.0 (N_2)	-14.6	0.3	3.30	0.05	1.0 (Ar)	-8.10	0.05
	1.5 (N_2)	-14.5	0.3	3.27	0.05	1.5 (Ar)	-7.40	0.05
	2.0 (N_2)	-14.8	0.3	3.34	0.05	2.0 (Ar)	-6.80	0.05
	2.5 (N_2)	-15.5	0.3	3.50	0.05	2.5 (Ar)	-6.45	0.05
	3.0 (N_2)	-16.1	0.3	3.63	0.05			
	3.5 (N_2)	-17.1	0.3	3.86	0.05			

At the beginning of the ion flux density (I_0) measurements for arc evaporated thin films the influence of bias voltage was investigated. For bias voltages more negative than -30V, the probe current did not change further, which is an indication of the ion saturation region. Therefore all following measurements were carried out with a constant bias voltage of -50V.

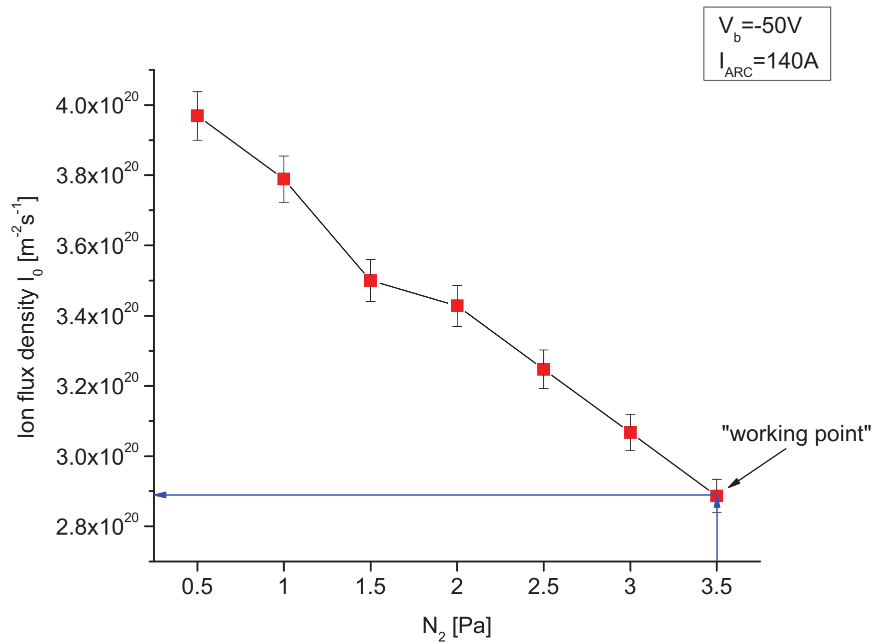

Fig. 5.19 Ion flux density I_0 of arc evaporated Al-Cr-N coatings

Fig. 5.19 shows the ion flux density for an arc current of 140A. In this experiment the nitrogen content was gradually increased up to 3.5 Pa. From this illustration it can be seen that with raising nitrogen the ion flux is decreased. The irregularity in the graph is attributed to the fluctuations of the ampere meter.

With a nitrogen pressure of 3.5 Pa and 140A (“working point”) an ion flux density I_0 of about $2.9x10^{20} m^{-2} s^{-1}$ is reached. In addition the ion flux density was measured at a pressure of 1Pa Ar and N_2, respectively, as a function of arc current (Fig. 5.20). Increasing the arc current from 100A to 200A results for both, Ar or N_2 environment, in a probe current about three times higher than for 100A.

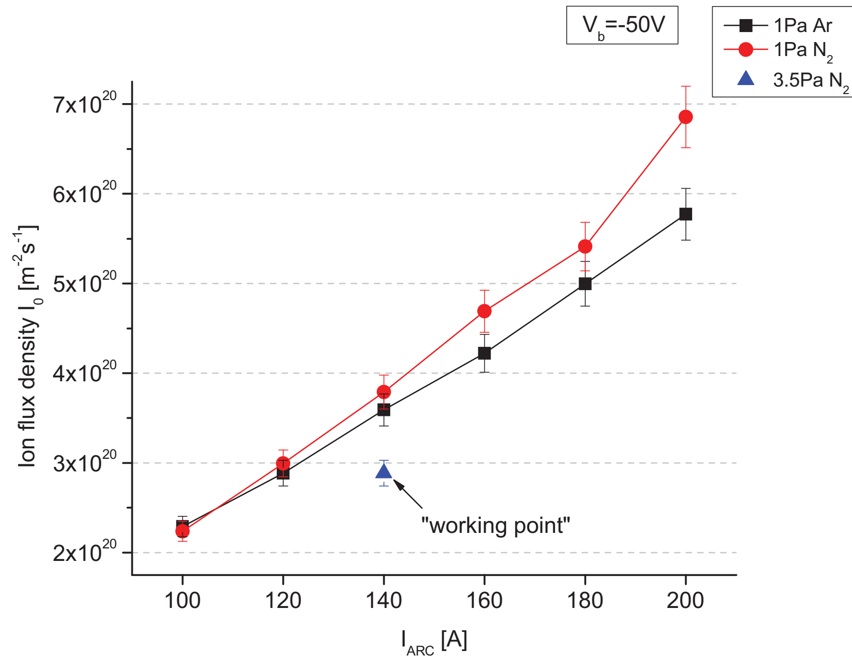

Fig. 5.20 Ion flux density as a function of arc current and ambient gas

With the known ion flux density and incorporation rate the ion assistance α was calculated. The ion assistance of arc evaporated Al-Cr-N coatings is in the range of 1.15 to 1.8, illustrated in Fig. 5.21. It can be seen that with rising substrate voltage and aluminium fraction the ion assistance increases. The obtained values for the ion assistance are close to one, due to the high ionization degree of arc evaporation.

Furthermore the mean plasma density (n_i) of arc evaporated Al-Cr-N thin films, deposited within this diploma thesis, has been determined. The plasma density increases with decreasing Cr fraction and ranges from $1.75x10^{17}\,m^{-3}$ to $2.1x10^{17}\,m^{-3}$.

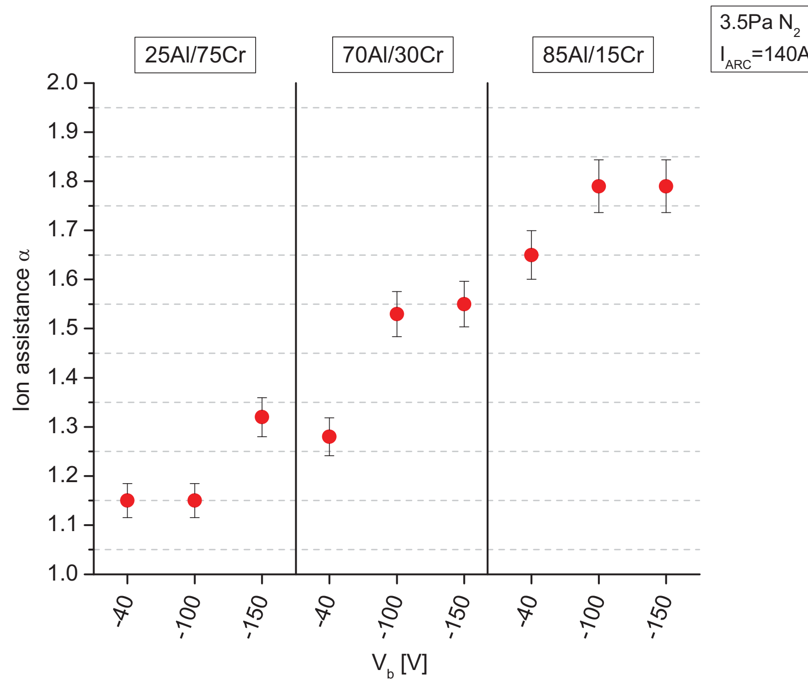

Fig. 5.21 Ion assistance of arc evaporated Al-Cr-N thin films

5.6.3 Comparison of arc evaporated and sputtered coatings

Looking at the incorporation rate of both magnetron sputtering and arc evaporation, it can be seen that $J_{Al\&Cr}$ of the arced Al-Cr-N coatings is about five to ten times higher. Therefore the growth rate of arc evaporated Al-Cr-N is much higher than for the sputtered one. But the evaluation of the incorporation rate also manifested a sharp rise in sputtering with increasing chromium content. As a result, the incorporation rate of sputtered Al-Cr-N thin films has been quadrupled while arc evaporated coatings showed only an increase of 50% for the used target compositions. Comparing the floating potential of both methods as it appears during the coating process, similar values were measured. The magnetron sputtering and arc evaporation process supply a potential of -15.4V and -17.1V respectively. Additionally it must be said that the bias applied during deposition was negative (the used coating plant only provides negative bias voltage). That means the working area referred to the voltage-current characteristics is the ion saturation region, in which the electrons arriving at the probe are repelled. After determining the floating potential, the probe current was measured to get information about the amount of the ion flux I_0.

For arc evaporation the ion flux density is about three times higher than for magnetron sputtering. As a result of this measurement it can be said that for bias voltages more negative than -30V no significant dependence was identifiable. Increasing the nitrogen partial pressure resulted in a decrease of the ion flux whereas an increase of arc current or sputter power resulted in higher densities. As consequence the amount of ions depends on the arc current or sputter power applied and of course on the total gas pressure in the coating chamber (recombinations). This is in good agreement with Mayrhofer et al. [14].

Conferring the ion assistance higher values were obtained for magnetron sputtering, since the lower ion flux density for this technique coincides with an even lower incorporation rate. However, the different ionized species in magnetron sputtering (Ar and N) and arc evaporation mode (N, Al, Cr) need to be considered. While for the first predominantly gas ions are present the flux from an arc discharge comprises to a large part also metal ions with the effect that their contribution decreases the apparent assistance by artificially increasing the incorporation rate. Also the impulse transfer from Ar or N to Al, Cr for the magnetron sputtering mode is less efficient as the metal-metal impulse transfer present in arc mode, which might partially offset the lack in ion assistance for the latter.

6 Summary

Within this thesis, a comparative study of Al-Cr-N films synthesized by reactive magnetron sputtering and arc evaporation was carried out. Al-Cr-N is a well established coating system with good oxidation and wear resistance. In this work investigations of coating morphology, XRD measurements for the characterization of the structure and phase composition, hardness measurements, beam bending tests for the determination of residual stresses, and plasma measurements were made. For these tests, three different AlCr targets with an Al content ranging from 25 over 70 up to 85at% were used. The thin films were deposited using an industrial scale rapid coating system (RCS) plant from Oerlikon Balzers Coating.

Al-Cr-N is a ternary nitride coating system with good mechanical properties and due to its excellent oxidation and wear resistance it is a promising compound for application on, e.g., cutting tools. Furthermore, the thermal stability ranges up to 1000°C and is as such surpassing most of the common hard coatings [4, 60]. For the deposition of Al-Cr-N films, reactive magnetron sputtering and cathodic arc evaporation were used. From economical view, arc evaporation is established as the most common industrial synthesis route, due to its high ionisation degree and because of the high deposition rates. On the other hand, during arc evaporation macroparticles are deposited and these droplets deteriorate mechanical properties and increase surface roughness. Magnetron sputtering in turn is droplet free, but provides only moderate deposition rates and the ionization degree is also low. The assignment of this study was to characterise and compare the synthesis conditions as well as their effect upon structure and properties of the coatings synthesized by the two techniques. By varying the target composition, and deposition parameters such as bias voltage and nitrogen pressure, different effects on evolution of the coating structure have been observed.

The arc evaporated and sputtered Al-Cr-N thin films were deposited on high speed steel substrates and additionally on silicon substrates with (100) orientation and a thickness of about 525 microns. During deposition, the substrate temperature was held constant at 500°C. With the arc evaporation method, the arc current was adjusted with 140A (~2.8 kW) and the nitrogen pressure was maintained at 3.5 Pa (100%). With magnetron sputtering, a power of 4 kW (26 Wcm^{-2}) was supplied and the gas pressure was adjusted with 1 Pa, consisting of argon and 25% nitrogen. All coatings were synthesized in stationary mode. Furthermore, the bias voltage applied was varied between -40V and -150V.

Comparing the deposition rates of arced and sputtered coatings it can be seen that the rate of arc evaporated films is much higher. The deposition rate decreases with increasing Al content and with rising bias voltage.

SEM micrographs revealed a more dense morphology for the arc evaporated coatings. With the help of a white light interferometer, the surface roughness R_a of the arc evaporated Al-Cr-N films has been measured indicating that the thickness equivalent roughness decreases with increasing aluminium fraction. Additionally the droplet size diminishes with increasing aluminium content.

The crystalline phases were identified by X-ray diffraction. With an Al/Cr target ratio of 25/75, only reflexes of the cubic $Al_{1-x}Cr_xN$ phase have been found for both sputtered and arc evaporated coatings. In the sputtered films, a transition from preferred (111) to (200) orientation of the cubic phase with decreasing bias voltage was observed. An increasing Al/Cr ratio (70/30) in the target results in formation of a phase mixture consisting of hexagonal and cubic $Al_{1-x}Cr_xN$ at low bias voltages. However, in the arced coatings the hexagonal phase fraction is much higher compared to the sputtered one, as obtained by Rietveld refinement. Increasing the bias voltage up to –100 V and even further up to –150 V, only the cubic phase is formed. For this target composition, a partial transition from the cubic to the hexagonal structure can be observed, due to the solubility limit of AlN (~70%) in CrN. This is in good agreement with the results reported from Sugishima et al. [66]. Using the 85Al/15Cr target, the hexagonal $Al_{1-x}Cr_xN$ phase is predominant and at higher bias voltage this phase shows a preferred (100) orientation. Rietveld refinement have also indicated that the lattice constant of the cubic phase decreases with increasing Al fraction. Considering the hexagonal –structure, the lattice constants increase in both directions (a- and c-direction) with increasing aluminium fraction.

According to the respective dominant coating structure, varying mechanical properties have been obtained. Hardness measurements, carried out by Vickers micro-indentation, have shown that the highest hardness values were obtained for the 70Al/30Cr target and dominating cubic structure, reaching a hardness (HU_{pl}) and an elastic modulus of approximately 28 GPa and 320 GPa, respectively. Generally, magnetron sputtered coatings revealed higher hardness values. Likewise, higher hardness values have also be found for both deposition techniques for increasing bias voltages. Beam bending tests for residual stress measurements revealed a similar behaviour as the hardness measurements, i.e. the compressive stresses (up to -6 GPa) also increase with rising bias voltage, due to the increasing defect density caused by the higher energy of the ions bombarding the growing film.

To compare magnetron sputtering and arc evaporation, the particle incorporation rate, the floating potential, and the ion flux density were measured. The incorporation rate of arc evaporated coatings is about five to ten times higher than for sputtered films. The floating potential in magnetron sputtering and arc evaporation for the standard deposition parameters is -15.4 V and -17.1 V, respectively. This results in a electron temperature of 3.36 eV and 3.86 eV, respectively. Generally, the floating potential becomes more negative with increasing sputtering power, arc current, and gas pressure. The ion flux density was measured using flat plasma probes. These measurements revealed that in the arc evaporation mode, the ion flux density is about three times higher than for magnetron sputtering and, therefore, also the ion saturation current in the arc evaporation mode is approximately three times higher. With decreasing deposition rate and nitrogen gas pressure, the ratio between impinging ions and deposited atoms rises. The ion assistance, being the ion/atom flux ratio and a measure for the efficiency of ion bombardment, of magnetron sputtered coatings is, however, higher compared to arc evaporation, due to the lower ionization degree in comparison to arc evaporation.

In summary, this thesis provides a solid basis for a comparison of the two main physical vapour deposition techniques, i.e. magnetron sputtering and cathodic arc evaporation, for Al-Cr-N coatings. It reveals that on the one hand, arc evaporation is the more economic process with higher deposition rates, higher ionisation rates and thus denser coatings, however, magnetron sputtering results in smoother coatings without inherent macro-particles.

7 List of tables and figures

7.1 List of tables

Table 4.1 Constant parameters during magnetron sputtering 28

Table 4.2 Magnetron sputtered coatings 29

Table 4.3 Constant parameters during arc evaporation 29

Table 4.4 Arc evaporated coatings 30

Table 4.5 Diffraction parameters 34

Table 5.1 Parameters influencing the deposition rate in sputtered thin films 44

Table 5.2 Parameters influencing the deposition rate in arced coatings 45

Table 5.3 Thickness and growth rate of sputtered Al-Cr-N coatings 46

Table 5.4 Thickness and growth rate of arced Al-Cr-N coatings 46

Table 5.5 Preferred orientation and texture coefficient of synthesized AlCrN films...53

Table 5.6 Floating potential and electron temp. in 1 Pa (25%N_2) environment 67

Table 5.7 Floating potential and electron temperature in 1 Pa Ar environment.........67

Table 5.8 Floating potential and electron temperature in 1 Pa N_2 environment……. 67

Table 5.9 Floating potential as a function of arc current (constant pressure)............71

Table 5.10 Floating potential as a function of gas pressure 71

7.2 List of figures

Fig. 2.1 Voltage-current characteristic of a gas discharge [6] 6

Fig. 2.2 Illustration of an voltage-current curve [15] 8

Fig. 2.3 Sputtering process 11

Fig. 2.4 Schematic illustration of the sputtering source in planar configuration [20]..12

Fig. 2.5 Linear collision cascade regime 13

Fig. 2.6 Planar magnetron configuration [14] 14

Fig. 2.7 Arc evaporation deposition configurations [24] 16

Fig. 2.8 Cathodic arc discharge process [9]...17

Fig. 3.1 Formation of a thin layer [16] 19

Fig. 3.2 Growth modes [10]..20

Fig. 3.3 Structure zone model after Thornton [34]..22

Fig. 3.4 Revised structure zone model after Messier [36] 22

Fig. 4.1 RCS-plant from Oerlikon Balzers, without substrate carrousel 24

Fig. 4.2 Schematic of Balzers RCS coating system, including substrate carrousel...25

Fig. 4.3 Deposition chamber [38] 26

Fig. 4.4 „Balinit Editor“ 27

Fig. 4.5 Ball cratering method [14, 41] 31

Fig. 4.6 White Light Interferometer [16]..33

Fig. 4.7 Principle of X-ray diffraction [46] 34

Fig. 4.8 Bent coating substrate composite [14] 35

Fig. 4.9 Principle of the stress measurement [14] 36

Fig. 4.10 Load indentation curve..37

Fig. 4.11 Ion probe arrangement...40

Fig. 4.12 Schematic view of a probe 40

Fig. 4.13 Circuit diagram of plasma measurements...41

Fig. 5.1 Abrasion crater...43

Fig. 5.2 SEM of a magnetron sputtered coating...47

Fig. 5.3 SEM of an arc evaporated coating 48

Fig. 5.4 3D-plot of an arc evaporated coating surface 49

Fig. 5.5 Thickness equivalent roughness of arced thin films 50

Fig. 5.6 XRD patterns of synthesized Al-Cr-N thin films using the 25Al/75Cr target .52

Fig. 5.7 XRD patterns of synthesized Al-Cr-N thin films using the 70Al/30Cr target .52

Fig. 5.8 XRD patterns of synthesized Al-Cr-N thin films using the 85Al/15Cr target .52

Fig. 5.9 Rietveld phase composition of Al-Cr-N coatings 55

Fig. 5.10 Stress vs. temperature of Al-Cr-N deposited on Si (100) substrate...........57

Fig. 5.11 Residual stresses in Al-Cr-N coatings deposited on Si (100) substrate 58

Fig. 5.12 Linear thermal expansion coefficient (α) of Al-Cr-N thin films 60

Fig. 5.13 Hardness and young modulus of sputtered Al-Cr-N coatings 62

Fig. 5.14 Hardness and modulus of arced Al-Cr-N coatings 63

Fig. 5.15 Incorporation rate of magnetron sputtered Al-Cr-N coatings......................66

Fig. 5.16 Ion flux density I_0 of magnetron sputtered Al-Cr-N coatings.......................68

Fig. 5.17 Ion assistance of magnetron sputtered Al-Cr-N coatings 69

Fig. 5.18 Incorporation rate of arc evaporated Al-Cr-N coatings 70

Fig. 5.19 Ion flux density I_0 of arc evaporated Al-Cr-N coatings...............................72

Fig. 5.20 Ion flux density I_0 as a function of arc current and ambient gas 73

Fig. 5.21 Ion assistance of arc evaporated Al-Cr-N thin films 74

8 References

1. M. Brizuela, A. Garcia-Luis, I. Braceras, J.I. Oñate, J.C. Sánchez-López, D. Martinez-Martinez, C. López-Cartes, A. Fernández, Surface and Coatings Technology 200 (2005) 192-197
2. J.C. Sánchez-López, D. Martinez-Martinez, C. López-Cartes, A. Fernández, M.Brizuela, A. Garcia-Luis, J.I. Oñate, Journal of Vacuum Science Technology A 23(4) (2005) 681-686
3. M. Kawate, A.K. Hashimoto, T. Suzuki, Surface and Coatings Technology 165 (2003) 163-167
4. H. Willmann, P.H. Mayrhofer, P.O.Å. Persson, A.E. Reiter, L. Hultman, C. Mitterer, *Thermal Stability of Al-Cr-N Hard Coatings*, Scripta Materialia 54 (2006) 1847-1851
5. J.R. Rooth, Industrial Plasma Engineering, Institute of Physics Publishing, Philadelphia (1995)
6. A. Bergauer, C. Eisenmenger-Sittner, *Physik und Technologie dünner Schichten*, www.ifp.tuwien.ac.at/forschung/duenne _schichten, (05.05.2006)
7. F.W. Bach, T. Duda, *Moderne Beschichtungsverfahren*, Deutsche Gesellschaft für Materialkunde e.V., WILEY-VCH Weinheim, Berlin (2000)
8. P. Losbichler, *Ultraharte PVD-Schichten im System Ti-B-N*, PhD thesis, University of Leoben (1998)
9. E.J.L. Rosén, *Theoretical and Experimental Studies Related to the Compositional and Microstructural Evolution of Alumina Thin Films*, PhD thesis, RWTH Aachen University (2004)
10. H. Willmann, *Hochtemperatureigenschaften nanokristalliner PVD-Hartstoffschichten*, Diploma thesis, University of Leoben (2001)
11. G. Franz, *Oberflächentechnologie mit Niederdruckplasmen*, Springer-Verlag, Berlin Heidelberg (1994)
12. Structure of glow discharge, http://science-education.pppl.gov/SummerInst/SGershman/Structure_of_Glow_Discharge.pdf, (09.05.2006)
13. Hartmut Frey, *Vakuum-Beschichtung 1*, VDI-Verlag, Düsseldorf (1995)
14. P.H. Mayrhofer, *Materials Science Aspects of Nanocrystalline PVD Hard Coatings*, PhD thesis, University of Leoben (2001)
15. Thomas Welzel, *Plasmadiagnostische Charakterisierung der Magnetronentladung zur c-BN-Abscheidung*, PhD thesis, TU Chmenitz (1998)
16. P.H. Mayrhofer, *Materials Science of Hard Coatings*, lecture script, University of Leoben (2003)
17. J. D. Callen, *Fundamentals of Plasma Physics*, University of Wisconsin (2003)

18. *Plasma potential and floating potential*, http://www.elettra.trieste.it/, (18.10.2006)
19. Scientific Systems, www.scisys.com, (24.10.2006)
20. R.A. Haefer, *Oberflächen- und Dünnschicht-Technologie, Teil 1, Beschichtungen von Oberflächen*, Springer-Verlag, Berlin (1987)
21. Gregory F. Spencer, Sputtering, Texas State University, Department of physics, http://uweb.txstate.edu/~gs14/5324/sputter_1.pdf, (07.11.2006)
22. *Der reaktive DC-Magnetron Sputterprozess*, http://ia.physik.rwth-aachen.de/research/sputtering/www-sputter-de.pdf, (29.11.2006)
23. D. Güttler, Mechanisms of Target Poisoning…, Annual Report IIM 2004, FZR 427, 34-37
24. D. M. Mattox, Vacuum Deposition Processes, www.pfonline.com/articles/069901.html (25.08.2005)
25. R. L. Boxman, S. Goldsmith, Surface and Coatings Technology 52 (1992) 39-50
26. A. Anders, IEEE Transactions on Plasma Science 29 (2) (2001) 393-398
27. W-D Münz, I.J. Smith, D.B. Lewis, S. Creasey, Elsevier Science Ltd., 48 (5) (1997) 473-481
28. D.M. Sanders, ASM Handbook Volume 5, Surface Engineering, ASM International (1994) 602-604
29. R.F. Bunshah, *Handbook of Deposition Techniques for Films and Coatings*, Noyes Publications, 2nd Edition (1994) 27-54
30. A.R.P. de Ataide, C. Alves Jr., V. Hajek, J.P. Leite, Surface and Coatings Technology 167 (2003) 52-58
31. Peter Deák, MST05 http://surphy.fat.bme.hu/pub/MaterSci/T05.DOC.pdf, (2005) 61-64
32. I. Petrov, P.B. Barna, L. Hultman, J.E. Greene, J. Vac. Sci. Technol. A, 21(5) (2003) 117-128
33. B.A. Movchan, A.V. Denchisin, Phys. Metals Metallogr., 28 (1969) 83
34. J.A. Thornton, Ann. Rev. Mater. Sci. 7 (1977) 239
35. M. Ohring, *Materials Science of thin films*, Academic Press, San Diego (2002)
36. R. Messier, A.P. Giri, R.A. Roy, J. Vac. Sci. Technol. A, 2(2) (1984) 500
37. *Thin Film Deposition and Applications*, CEI-Europe Advanced Technology Education, Uppsala Sweden (2003) 104
38. Oerlikon Balzers Coating, http://www.oerlikon.com, (Nov. 2006)
39. Plansee AG, http://www.plansee.com, (2006)
40. J. Neidhardt, M. O´Sullivan, A.E. Reiter, W. Rechberger, W. Grogger, C. Mitterer, Surface and Coatings Technology 201 (6) (2006) 2553-2559
41. DIN-EN 1071-2 (2003)

42. C. Kittel, *Einführung in die Festkörperphysik*, Oldenbourg Wissenschaftsverlag München, (1993)
43. Profilometer, University of Leoben, Thin Films Group, http://www.unileoben.ac.at, (2006)
44. R. Allmann, Röntgenpulverdiffraktometrie, Springer Verlag, Berlin (2003) 96
45. D.L. Bish, J.E. Post, *Modern Powder Diffraction*, Reviews in Mineralogy 20 (1989) 1-26
46. Röntgendiffraktometer, University of Leoben, Thin Films Group, http://www.unileoben.ac.at, (2006)
47. PDF-2 Data Base Sets 1-45, JCPDS – International Centre for Diffraction Data (1995)
48. G.B. Harris, Phil. Mag., 43 (1952) 113-122
49. R.A. Young, *The Rietveld method*, Oxford University Press, Oxford (1993)
50. Bruker AXS GmbH, http://www.bruker-axs.com (2006)
51. D. Winkler, *Konzeption und Realisierung eines thermisch unterstützten Messverfahrens zur Bestimmung von Eigenspannungen in dünnen Schichten*, Diploma thesis, University of Leoben (1997)
52. J.D. Wilcock, D.S. Campbell, Thin Solid Films 3 (1969) 3-12
53. G.C.A.M. Janssen, Thin Solid Films 515 (17) (2007) 6654-6664
54. M.D. Larsson, P. Hedenquist, S. Hogmark, Surface Engineering, 12 (1) (1996) 43-48
55. H. Ebert. In: K. Schäfer and G. Beggerow, Editors, *Landolt-Börnstein Eigenschaften der Materie in ihren Aggregatzuständen, 1. Teil, Mechanisch Thermische Zustandgrößen*, Springer, Berlin (1971), p. 402.
56. Helmut Fischer GmbH + Co.KG, http://www.Helmut-Fischer.com, (Nov. 2006)
57. A.C. Fischer-Cripps, P. Karvánková, S. Veprek, Surface and Coatings Technology 200 (2006) 5645
58. A.C. Fischer-Cripps, Surface and Coatings Technology 200 (14-15) (2006) 4153-4165
59. J.P. Booth, N.St.J. Braithwaite, A. Goodyear, F. Neuilly, J.-M. Francou, *Ion flux and electron temperature measurements with an insulator-covered planar electrostatic probe*, http://crppwww.epfl.ch/LTPD99/pdf/orals/booth2.pdf, (Dec. 2006)
60. R. Franz, B. Sartory, R. Kaindl, R. Tessadri, A. Reiter, V.H. Derflinger, P. Polcik, C. Mitterer, *High-temperature tribological studies of arc-evaporated $Al_xCr_{1-x}N$ coatings*, 16th International Plansee Seminar, Reutte, 2 (2005) 932-945
61. R. Wuhrer, W.Y. Yeung, Scripta Materialia 50 (2004) 1461-1466

62. Sputtering yields, http://www.angstromsciences.com/reference-guides/sputtering-yields/index.html, (Nov. 2006)
63. T. Hurkmans, D.B. Lewis, H. Paritong, J.S. Brooks, W.D. Münz, Surface and Coatings Technology 114 (1999) 52-59
64. E. Lugscheider, K. Bobzin, Th. Hornig, M. Maes, Thin Solid Films 420-421 (2002) 318-323
65. P.Eh. Hovsepian, C. Reinhard, A.P. Ehiasarian, Surface and Coatings Technology 201 (2006) 4105-4110
66. A. Sugishima, H. Kajioka, Y. Makino, Surface and Coatings Technology 97 (1997) 590-594
67. Y. Makino, K. Nogi, Surface and Coatings Technology 98 (1998) 1008-1012
68. P.H. Mayrhofer, D. Music, J.M. Schneider, Applied Physics Letters 100, 094906 (2006)
69. C. Gautier, H. Moussaoui, F. Elstner, J. Machet, Surface and Coatings Technology 86-87 (1996) 254-262
70. J. Neidhardt, W. Ernst, H. Willmann, P. Mayrhofer, B. Sartory, C. Mitterer, in manuscript
71. Y.Ide, T. Nakamura, K. Kishitake, Second International Conference on Processing Materials for Properties, 2000, 291-296
72. L. Hultman, *Growth of Single- and Polycrystalline TiN and ZrN Thin Films by Reactive Sputtering; Influence of Low Energy Ion Irradiation*, PhD thesis, Linköping University (1988)
73. S. Ulrich, H. Holleck, J. Ye, H. Leiste, R. Loos, M. Stüber, P. Pesch, S. Sattel, Thin Solid Films 437 (2003) 164-169
74. D.R. Lide, *Handbook of Chemistry and Physics*, 85th Edition CRC Press, Florida (2004-2005)
75. M. Kawate, A. Kimura, T. Suzuki, Journal of Vacuum Science Technology A 20 (2) (2002) 569-571
76. I. Petrov, I. Ivanov, V. Orlinov, J.-E. Sundgren, J. Vacuum Science Technology A 11 (5) (1993) 2733-2741
77. J.J. Olaya, S.E. Rodil, S. Muhl, L. Huerta, Surface and Coatings Technology 200 (2006) 5743-5750
78. R.L. Boxman, *Handbook of Vacuum Arc Science and Technology: Fundamental and Applications*, Noyes Publications, New Jersey (1995)